

Multi-Frequency Analysis of Fully Polarimetric Speckle Filter Based on Morphology Using Visual Quality Indices & Support Vector Machine

Akhil Masurkar

Department of Electronics Engineering
Veermata Jijabai Technological Institute (VJTI)
Mumbai, India
e-mail: aumasurkar_p18@el.vjti.ac.in

Rohin Daruwala

Department of Electronics Engineering
Veermata Jijabai Technological Institute (VJTI)
Mumbai, India
e-mail: aumasurkar_p18@el.vjti.ac.in

Varsha Turkar

Department of Electronics and Telecommunication Engineering
Vidyalankar Institute of Technology
Mumbai, India
e-mail: varshaturkar@ieee.org

Abstract—In this study the multifrequency data is utilized to test the performance of a novel fully polarimetric speckle filter based on Morphological operations. The main objective of this work is to determine the filter performance by inspecting the visual quality of the image using visual quality indices followed by a classification study on PolSAR images. PolSAR images are acquired from the P, L, & C bands of the Microwave range. The most commonly present noise in Polarimetric Synthetic Aperture Radar (PolSAR) images is the Speckle Noise. The speckle noise is removed using a novel fully polarimetric filter based on morphological operations. After Multi-looking the PolSAR images are converted into the Coherency Matrix commonly known as the T-Matrix. The Morphological filter is applied on the elements of the T-Matrix. Two opening and closing operations are considered while applying the Morphological filter to see the effect of multiple closing and opening operations. The opening and closing are based on the principles of erosion and dilation. The filtered images are then tested for visual quality and classification accuracies. The visual quality of the images after processing with morphological operations are carried out using the full reference & no reference quality metrics. The full reference quality metrics considered are Mean Square Error (MSE), Peak Signal to Noise Ratio (PSNR), Structural Similarity Index (SSIM) and Multi-Scale Structural Similarity Index (MS-SSIM). The no reference quality metrics considered are Blind/Reference less Image Spatial Quality Evaluator (BRISQUE), Natural Image Quality Evaluator (NIQE), and Perception based Image Quality Evaluator (PIQE). The commonly used edge preservation index for SAR images is also calculated. The classification accuracy is determined using the Support Vector Machine (SVM), with Radial Basis Function (RBF) as the kernel, along with cross validation. The visual quality of the image and the classification accuracies are compared with the existing filters at all the P, L, & C band frequencies. It is observed that the proposed technique can reduce the speckle significantly, maintain visual quality and give good classification accuracies, at all the three frequencies..

Keywords-Multi-frequency, SAR, Morphology, Speckle Filtering, Support Vector Machine, Classification

I. INTRODUCTION

Synthetic Aperture Radar (SAR) is an active high-resolution imaging sensor. It can perform in all weather and operate during the day as well as night. The primary source of noise in all SAR systems is the speckle noise. This is mainly due to the use of a coherent imaging system. Speckle has characteristic of a multiplicative noise and shows granular pattern in the image. The speckle greatly affects the quality of SAR images. It makes subsequent image segmentation, region of interest extraction, target detection, target recognition and classification, etc. difficult. Hence removal of speckle noise becomes a crucial pre-processing step in all SAR applications. A good speckle filter must be able to reduce the speckle significantly while preserving the resolution and structural details. Generally, speckle filters are designed by selecting enough samples with closely similar scattering properties and the construction of an unbiased estimator.

Boxcar is the simplest filter which locates similar pixels by a moving window with a predefined size. It can reduce the speckle however significant blurring is observed. Filters like the Lee filter, Frost filter, Kuan filter and Sigma filter [1-2] have been developed by utilizing statistical properties like local pixel intensity. The refined Lee filter [3-4] shows good performance especially for edge preservation. Improved Sigma filter [7] can select unconnected pixels for a given sigma range while strong targets remain unfiltered. The solution to the above problems was the use of nonlocal means algorithm [6]. However, the applications of the same are limited because of computational burden and low efficiency caused by similar search steps. Transform domain filters such as the [5] wavelet-based threshold filters use wavelet transformation which can separate signals into high and low frequency parts. The speckle usually belongs to high frequency component and hence can be removed. SAR-BM3D algorithm [8] is one of the best transform domain methods, which combines the nonlocal idea with transform domain filters. However, its efficiency is low since it deploys many search operations. Filters using a variational approach [9-10] have achieved good performance in SAR image de-speckling, but the result is usually dependent on the choice of the model parameters. After any kind of filtering the visual quality of the image gets affected. Hence it is important to inspect the visual quality of the image using quality indices. Speckle filtering is often followed by classification studies. It is expected that the filtering technique should improve the classification accuracies.

The visual quality of the images is mostly determined using Full reference Quality Metrics, No Reference Quality Metrics and Edge Preservation index. The Full reference Quality Metrics are Mean-squared error (MSE), Peak signal-

to-noise ratio (PSNR), Structural Similarity Index (SSIM) & Multi-scale Structural Similarity Index (MSSIM). The No-reference quality metrics are Blind/Reference less Image Spatial Quality Evaluator (BRISQUE), Natural Image Quality Evaluator (NIQE) and Perception based Image Quality Evaluator (PIQE).

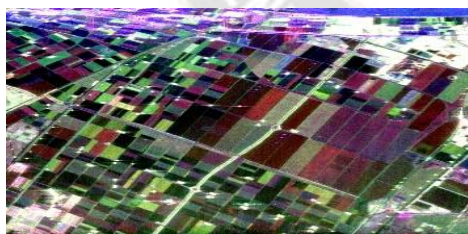
The quality assessment of filtering technique is truly incomplete without a classification study. It is expected that the classification accuracies should be high after applying filtering techniques. The most used classifiers are Random Forest, K- Nearest Neighbors and Support Vector Machine (SVM).

Random Forest is an ensemble machine learning technique that produces multiple decision trees. It is a collection of many decision trees and decides the output of the model by majority vote. Using a greater number of trees can fetch us a very accurate model. However, using more trees than required can consume a large amount of time, without significant improvement in the model parameters.

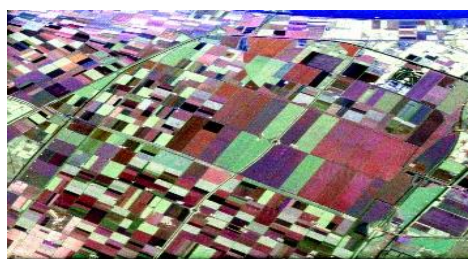
K - Nearest Neighbors (KNN) is an algorithm that works by assuming that elements of a similar class lie close to each other. KNN algorithm is non-parametric in nature. The different methods to calculate the distance of the point of interest (target point) from the 'k' number of neighbors are Euclidean, Manhattan, Chebyshev, and Mahalanobis. However Euclidean distance is most widely used. After calculating the distance from 'k' neighbors, the majority vote is considered, and the target point is assigned to the class for which the number of neighbors is maximum. KNN is often called a lazy learner because the training period is high as compared to other machine learning models. This is because KNN algorithm must calculate distance from every point in its neighborhood. If the number of points is substantially higher then, the time taken to train the model can be even higher.

Support Vector Machine (SVM) is a machine learning technique used in classification problems and regression analysis. SVM uses an optimal hyper-plane that has a maximum distance from the data points of two classes. The most important parameter in SVM classifier is the kernel function. The purpose of using the kernel function is to transform the dataset from a non-separable dataset to a separable one. Both SVM and KNN algorithms are based on grouping and separability (Marrs and Ni-Meister, 2019). The most used kernel functions are the polynomial and radial bias function (RBF). The polynomial kernel function works well with a fewer number of classes and whereas the RBF kernel function is preferred when the number of classes are significantly higher.

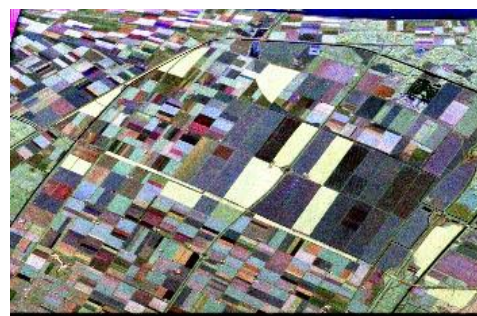
In the present work the multifrequency data is utilized to test the performance of the Fully Polarimetric Speckle Filter based on Morphological operations. The main objective of this work is to determine the filter performance by inspecting the visual quality of the image using visual quality indices followed by a classification study on PolSAR images. The visual quality of the images after processing with morphological operations are carried out using the full reference quality metric, no reference quality metric and the edge preservation index. The classification accuracy is determined using the Support Vector Machine (SVM), with Radial Basis Function (RBF) as the kernel, along with cross validation. Multi-frequency SAR data is used for generating accurate land cover maps. Section II illustrates the use of Morphology on SAR images. Section III discusses complete workflow beginning from preprocessing the data to the final classified image which includes visual quality analysis using quality indices and working of Support Vector Machine (SVM) applied to the filtered images. Section 4 presents the results and evaluation metrics comparing the performance for land cover classification using multifrequency spaceborne fully polarimetric SAR data. The PolSAR images correspond to the frequencies of the P, L & C Band of the Microwave range, from the AIRSAR satellite, which is an AIRBORNE satellite. The data is Quad Pol fully polarized. The swath is 10km and the off-nadir angle is 20°-60°. The frequency /wavelengths of the P, L and C band images are 0.45GHz/67cm, 1.26GHz/23cm&5.31GHz/5.7cm respectively. The range resolution for the P, L and C Band images is 7.5m, 3.75m and 1.875m respectively. Images acquired are of the same region that is Flevoland, Netherlands. This data set is chosen since it has a good number of edges and point targets which are helpful in determining structural similarities.



(a) P-Band Image



(b) L-Band Image



(c) C-Band Image

Fig 1. Pauli RGB's of P, L & C Band Images

II. BASIC CONCEPT OF MORPHOLOGY

Morphology is a broad set of image processing operations which are used to process images based on the use of an image with a small shape or template called as the structuring element. In a morphological operation, each pixel in the image is adjusted based on the value of other pixels in its neighborhood. The structuring element is a small binary image, i.e., a small matrix of pixels, each with a value of zero or one. The matrix dimensions specify the size of the structuring element. The pattern of ones and zeros specifies the shape of the structuring element. The origin of the structuring element is usually one of its pixels, although generally the origin can also be outside the structuring element. Structuring elements generally have an odd dimension with the origin defined as the center of the matrix. Structuring elements play in morphological image processing the same role as convolution kernels in linear image filtering. The most used structural elements are diamond, disk, octagon, line, rectangle, square, & sphere. Specific shapes in the input image can be reconstructed by choosing the size and shape of the neighborhood. Morphological operations depend on the relative ordering of pixel values and not on their numerical values. Hence, they are especially suited to the processing of binary images.

A. Fundamental Operations

The basic operations in Morphology are erosion and dilation. Erosion reduces the size of the objects with respect to the background, eliminates the noise spikes & ragged edges, darkens the objects, and increases the size holes & sharpens the corners. Dilation on the other hand increases the size of the objects, eliminates noise spikes & ragged edges, brightens the objects, and connects objects, bridges gaps, smoothens edges, fills holes and creates outlines in an image.

A grey scale image is the input for the grey scale morphology operations. The mask moves across the image pixel by pixel, and the resultant is produced in the output

image. The structuring elements can be a square matrix of size 3x3, 5x5 or larger depending upon the application. Let 'A' be the given image and 'W' be the structuring element with mask weights as shown below.

$$W = \begin{bmatrix} 1 & 1 & 1 \\ 1 & 1 & 1 \\ 1 & 1 & 1 \end{bmatrix}$$

$$W = \begin{bmatrix} w_1 & w_2 & w_3 \\ w_4 & w_5 & w_6 \\ w_7 & w_8 & w_9 \end{bmatrix}$$

The eroded image is given by $E = A \ominus W$

$$E = A \ominus W$$

$$E = \min [w_1 * A(x-1, y-1), w_2 * A(x-1, y), w_3 * A(x-1, y+1), w_4 * A(x, y-1), w_5 * A(x, y), w_6 * A(x, y+1), w_7 * A(x+1, y-1), w_8 * A(x+1, y), w_9 * A(x+1, y+1)]$$

The numerical values of the point and its eight neighbors are evaluated and the minimal value among these nine replaces the value of the central pixel in the output image. The output value of the erosion process is the minimum value of all the nine factors for erosion.

The dilated image is given by $D = A \oplus W$

$$D = \max [w_1 * A(x-1, y-1), w_2 * A(x-1, y), w_3 * A(x-1, y+1), w_4 * A(x, y-1), w_5 * A(x, y), w_6 * A(x, y+1), w_7 * A(x+1, y-1), w_8 * A(x+1, y), w_9 * A(x+1, y+1)]$$

The numerical values of the point and its eight neighbors are evaluated and the maximum value among these nine replaces the value of the central pixel in the output image. The output value of the dilation process is the maximum value of all the nine factors for dilation.

B. Compound Operations

Many morphological operations are represented as combinations of erosion, and dilation. The opening operation erodes an image and then dilates the eroded image, using the same structuring element for both operations. Morphological opening is useful for removing small objects from an image while preserving the shape and size of larger objects in the image. The closing operation dilates an image and then erodes the dilated image, using the same structuring element for both operations. Morphological closing is useful for filling small holes from an image while preserving the shape and size of the objects in the image.

The opening of an image 'A' by a structuring element 'W' generates a new image 'O' which is denoted by

$$O = A \circ W$$

$$O = (A \ominus W) \oplus W$$

Opening is so called because it can open a gap between objects connected by a thin bridge of pixels. Any regions that have survived the erosion are restored to their original size by the dilation.

The Closing of an image 'A' by a structuring element 'W' generates a new image 'C' which is denoted by

$$C = A \bullet W$$

$$O = (A \oplus W) \ominus W$$

Closing is so called because it can fill holes in the regions while keeping the initial region sizes. It should be noted that opening and closing are idempotent operations.

$$(A \bullet W) \bullet W = A \bullet W$$

$$(A \circ W) \circ W = A \circ W$$

Once an image has been opened or closed, subsequent opening or closing operations with the same structuring element have no further effect on that image.

C. Morphological Filtering

Morphological filtering of a binary image is conducted by considering compound operations like opening and closing as filters. They may act as filters of shape. For example, opening with a disc structuring element smooths corners from the inside, and closing with a disc smooths corners from the outside. But also, these operations can filter out from an image any details that are smaller in size than the structuring element, e.g. opening is filtering the binary image at a scale defined by the size of the structuring element. Only those portions of the image that fit the structuring element are passed by the filter; smaller structures are blocked and excluded from the output image. The size of the structuring element is most important to eliminate noisy details but not to damage objects of interest.

III. METHODOLOGY

Synthetic Aperture Radar (SAR) is a side-looking sensor. The slant-range distortion causes the near-range objects to appear compressed relative to the far-range objects. This results in a nonlinear variation of captured image scale from near to far range. To overcome this problem multi-looking is performed. Multi-looking is the process in which square pixels are generated. The number of looks is determined from the image specifications. Pre-processing of SAR data, usually, involves radiometric calibration and multi-looking. The dataset used in this work was already calibrated so only multi-looking is performed.

A. Converting SAR Data Product to Coherency Matrix

Synthetic Aperture Radar (SAR) is an active high-resolution imaging sensor that can perform in all weather, and all-day

observations. Single and double polarization SAR systems have a good penetrating and active sensing capability. However, they have many limitations regarding determination of structural information about different targets which is essential during land use classification [13]. The polarimetric mode of the SAR system, on the contrary, provides SAR data from all the four polarization channels simultaneously, which is an advanced technique to extract the backscatter from various targets [14]. For a given radar cross -section the incident power density at the target to the reflected power density that results at the receiver is represented using the scattering matrix. The scattering matrix is used to identify the back scatter from an object after interaction with the incident electromagnetic radiation. Elements of the scattering matrix are complex numbers which account for both magnitude as well as phase information.

$$S = \begin{bmatrix} S_{VV} & S_{VH} \\ S_{HV} & S_{HH} \end{bmatrix}$$

The magnitude and phase values of all the four polarization channels of fully polarimetric SAR data are used to measure the complex elements of the scattering Matrix. In the case of AIRSAR fully polarimetric phased array synthetic aperture RADAR (PALSAR) monostatic antennas are used. Hence the scattering matrix becomes symmetric. Therefore, the effective scattering matrix elements become (S_{VV}, S_{HH}, S_{HV}) only instead of $(S_{VV}, S_{HH}, S_{HV}, S_{VH})$

Scattering information can be more conveniently represented by defining a target vector. This can be done with the help of a linear basis of feature vector (K_L) or a Pauli basis of feature vector (K_P). The linear basis of feature vector is known as lexicographic representation.

$$K_L = \begin{bmatrix} S_{HH} \\ \sqrt{2}S_{HV} \\ S_{VV} \end{bmatrix}$$

The Pauli basis of feature vector is known as lexicographic representation

$$K_P = \frac{1}{\sqrt{2}} \begin{bmatrix} S_{HH} + S_{VV} \\ S_{HH} - S_{VV} \\ 2 S_{HV} \end{bmatrix}$$

The above two basis of feature vectors are the main factors of the decomposition theories. Several matrices are defined to characterize the scattering properties of objects using a linear and Pauli basis of feature vector. The most widely used matrices are Covariance Matrix (C) and Coherency Matrix (T). The covariance matrix is defined as $C = K_L \cdot K_L^{*T}$, where * represents the conjugate and ^T represents transpose.

$$C = \begin{bmatrix} S_{HH} \cdot S_{HH}^* & \sqrt{2}S_{HH} \cdot S_{HV}^* & S_{HH} \cdot S_{VV}^* \\ \sqrt{2}S_{HV} \cdot S_{HH}^* & 2 S_{HV} \cdot S_{HV}^* & \sqrt{2}S_{HV} \cdot S_{VV}^* \\ S_{VV} \cdot S_{HH}^* & \sqrt{2}S_{VV} \cdot S_{HV}^* & S_{VV} \cdot S_{VV}^* \end{bmatrix}$$

The simplified form of the C Matrix are as follows

$$C = \begin{bmatrix} C_{11} & C_{12} & C_{13} \\ C_{21} & C_{22} & C_{23} \\ C_{31} & C_{32} & C_{33} \end{bmatrix}$$

The coherence matrix is defined as $T = K_P \cdot K_P^{*T}$, where * represents the conjugate and ^T represents transpose. The simplified form of the T Matrix are as follows:

$$T = \begin{bmatrix} T_{11} & T_{12} & T_{13} \\ T_{21} & T_{22} & T_{23} \\ T_{31} & T_{32} & T_{33} \end{bmatrix}$$

Each element of the T-Matrix is given as follows:

$$T_{11} = (S_{HH} + S_{VV})^2$$

$$T_{12} = (S_{HH} + S_{VV})(S_{HH} - S_{VV})^*$$

$$T_{13} = 2(S_{HH} + S_{VV})(S_{HV})^*$$

$$T_{21} = (S_{HH} - S_{VV})(S_{HH} + S_{VV})^*$$

$$T_{22} = (S_{HH} - S_{VV})^2$$

$$T_{23} = 2(S_{HH} - S_{VV})(S_{HV})^*$$

$$T_{31} = 2(S_{HV})(S_{HH} + S_{VV})^*$$

$$T_{32} = 2(S_{HV})(S_{HH} - S_{VV})^*$$

$$T_{33} = 4(S_{HV})^2$$

Coherency matrix is used in considered in this study since it is the more appropriate matrix representation of scattering where the phase of different combination of polarization is also considered.

B. Applying Morphological Filter on the PolSAR Images

The detailed steps to apply the morphological filter are given in figure 2.

Step1: Extract the T- Matrix (Coherency matrix) from the SAR data product.

Step 2: The structuring element (W) has size (3x3) and has following form

$$W = \begin{bmatrix} 1 & 1 & 1 \\ 1 & 1 & 1 \\ 1 & 1 & 1 \end{bmatrix}$$

Other structuring elements like $W = [1 \ 0 \ 1]$ or $W = [1 \ 1 \ 1]$ etc. can be used depending on the level of heterogeneity of targets in the PolSAR image.

Step 3: Morphological operations of opening followed by closing are performed twice, on each element of the

Coherency matrix with the structuring element as shown in figure above. From fig.3 it can be observed that morphological operations greatly help in enhancing the point targets.

Step 4: The images, difference images, histograms, and difference histograms, of each element of the T-matrix, after every erosion & dilation operation, are plotted to visually inspect the quality of the filtered image. Also, from fig.4 it can be observed that the difference histogram is largely black.

Step 5: A quantitative analysis of the visual quality of the images is then determined using Full reference Quality Metrics, No Reference Quality Metrics and Edge Preservation index. This is as shown in fig.5

Step 6: Create Pauli RGB image for visual inspection using the filtered elements of the coherency matrix (T-Matrix).

Step 7: Performed above operation on all the P, L & C Band images.

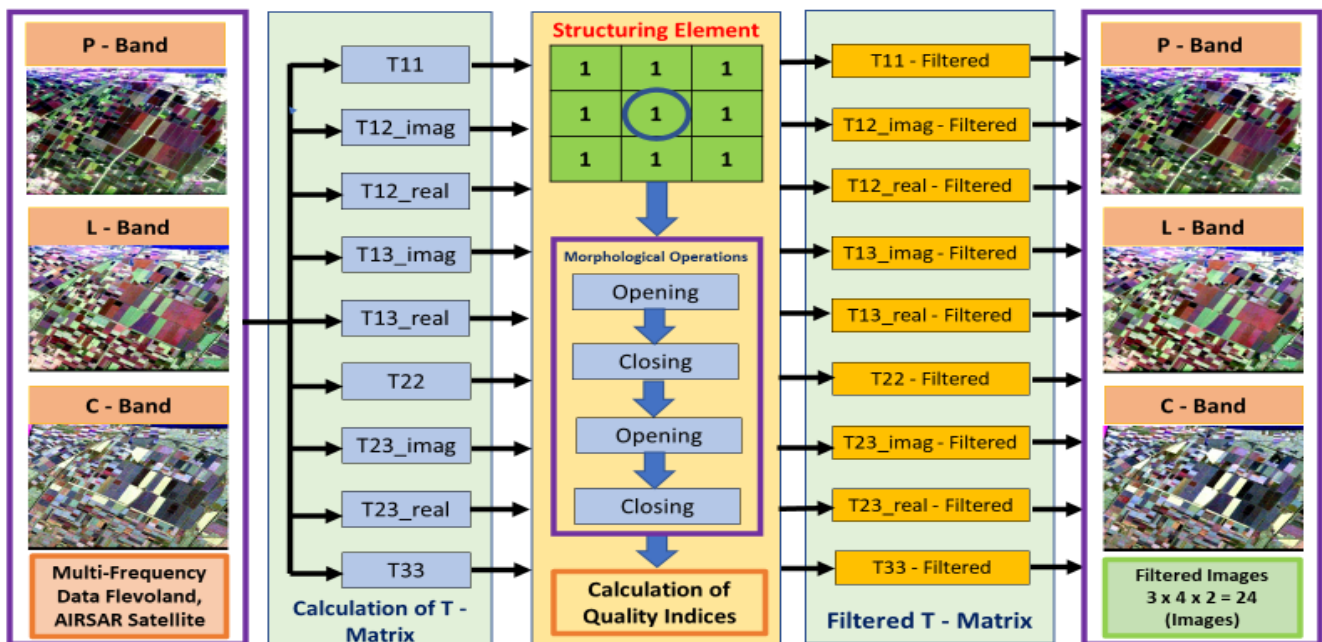


Fig 2: Method to apply Morphological filter on P, L & C Band PolSAR images

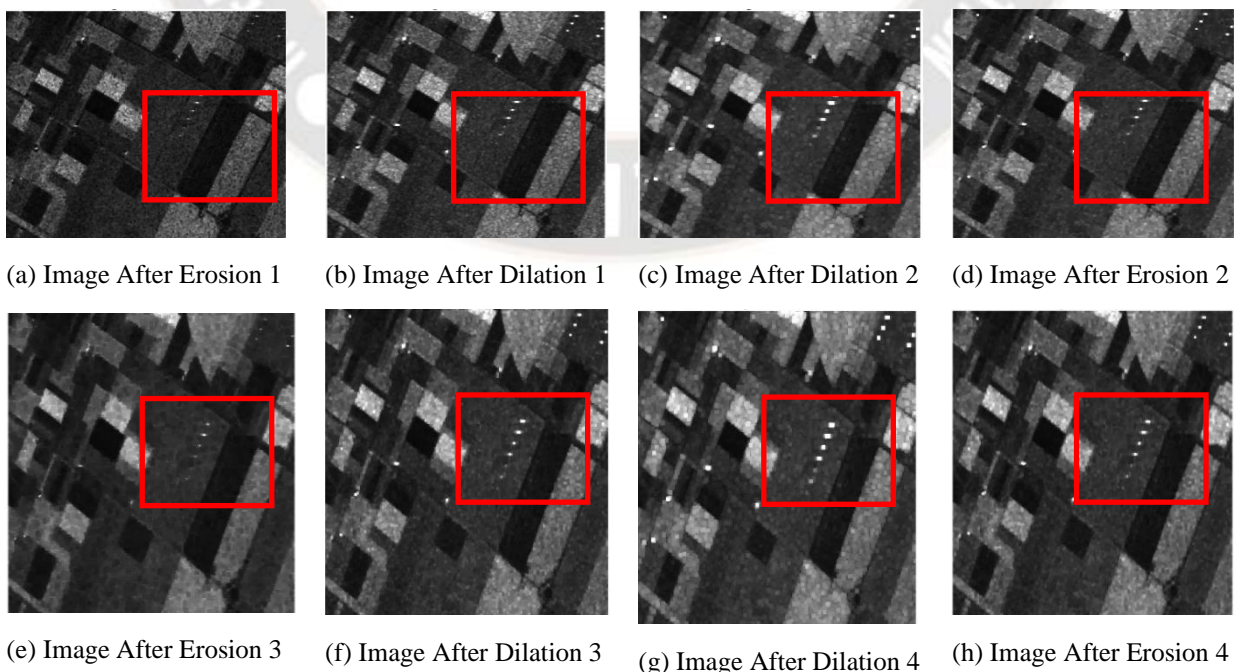


Fig 3: T11 Data of C- Band PolSAR image

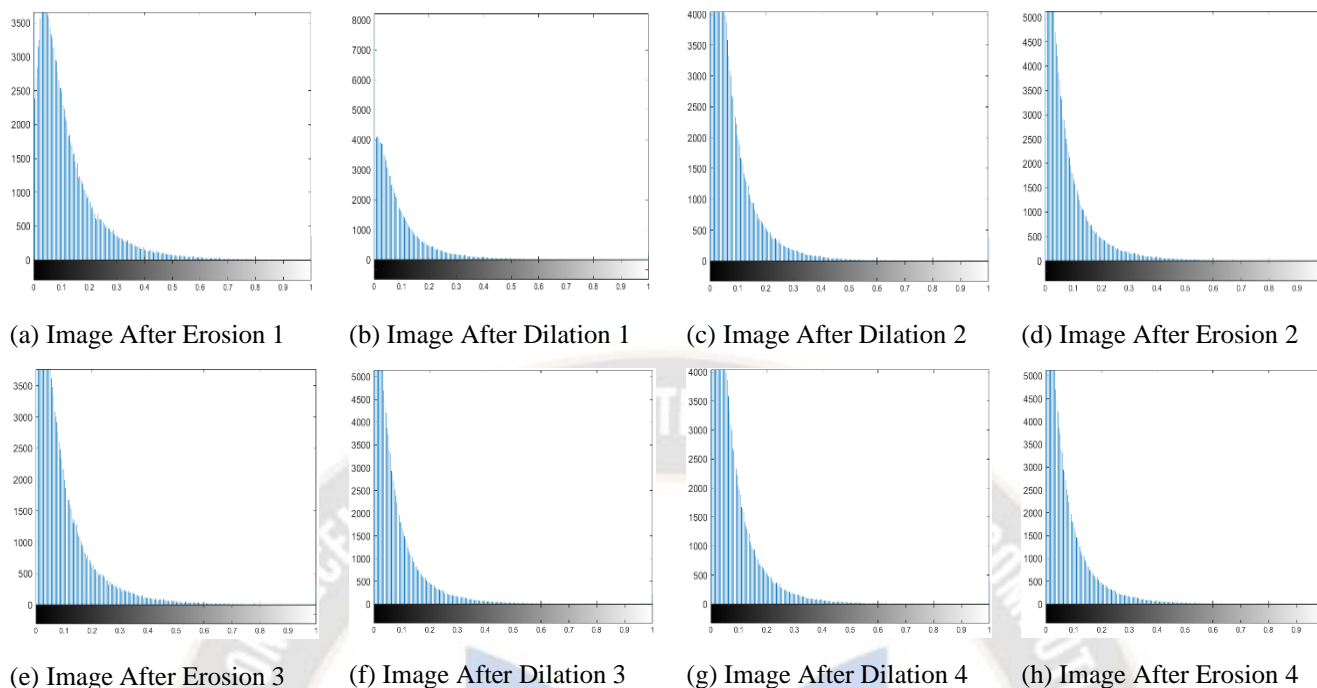


Fig 4: Difference Histogram for T11 data of C- Band PolSAR image after applying morphological operations

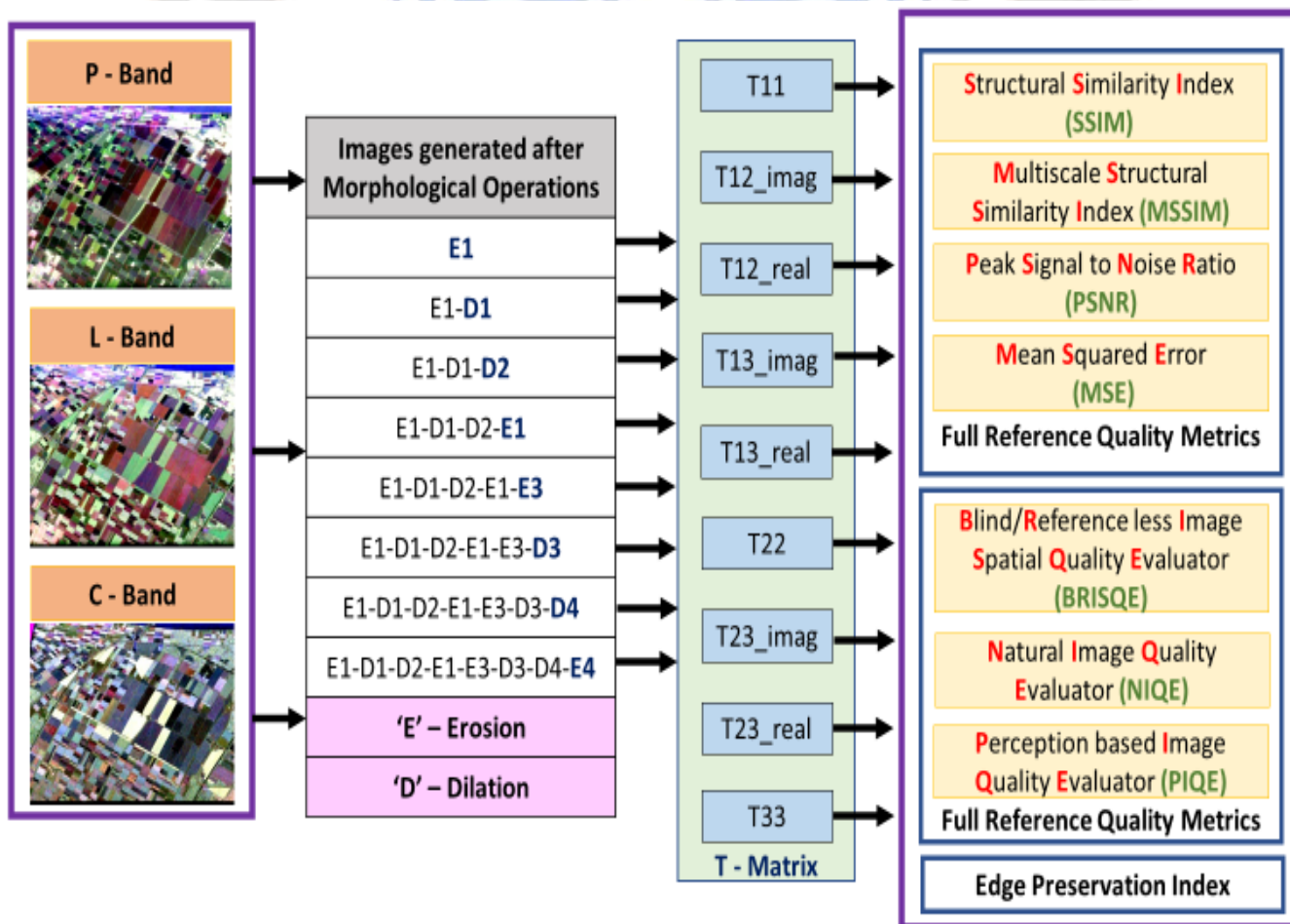


Fig 5: Visual quality of the images using Full reference No Reference and Edge Preservation indices

C. Applying other filters on the P, L, & C- Band Images

There is a need to compare the performance of the Morphological filter with other most used SAR filter. Hence the most common filters used in SAR image processing are also applied on the P, L & C images to compare the results with those images which are morphologically filtered. The steps to apply the most used filters is as shown in fig.6 and are as follows:

Step1: Extract the T- Matrix (Coherency matrix) from the SAR data product.

Step 2: Apply most used filters like Boxcar, Mean Shift, Gaussian, IDAN, Refined Lee, Lee Sigma, & Lopez Filter.

Step 3: A quantitative analysis of the visual quality of the images is then determined using Full reference Quality Metrics, No Reference Quality Metrics and Edge Preservation index.

Step 4: Create Pauli RGB image for visual inspection using the filtered elements of the coherency matrix (T-Matrix).

Step 5: Performed above operation on all the P, L & C Band images.

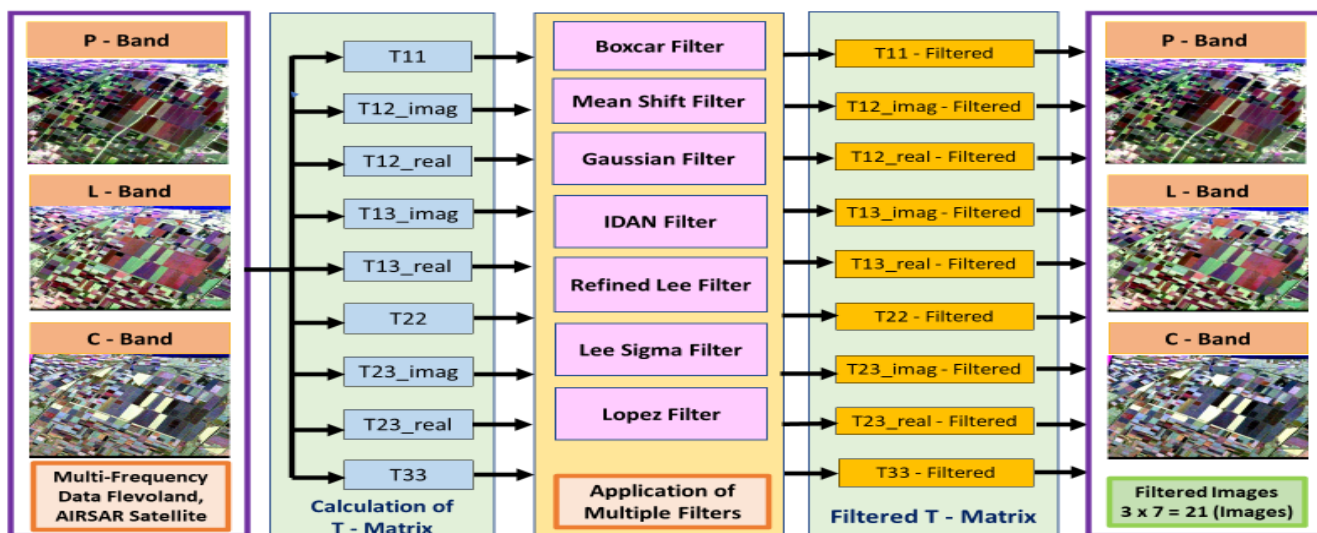


Fig 6: Method to apply Boxcar, Mean shift, Gaussian, IDAN, Refined Lee, Lee Sigma & Lopez filter on P, L & C band PolSAR images

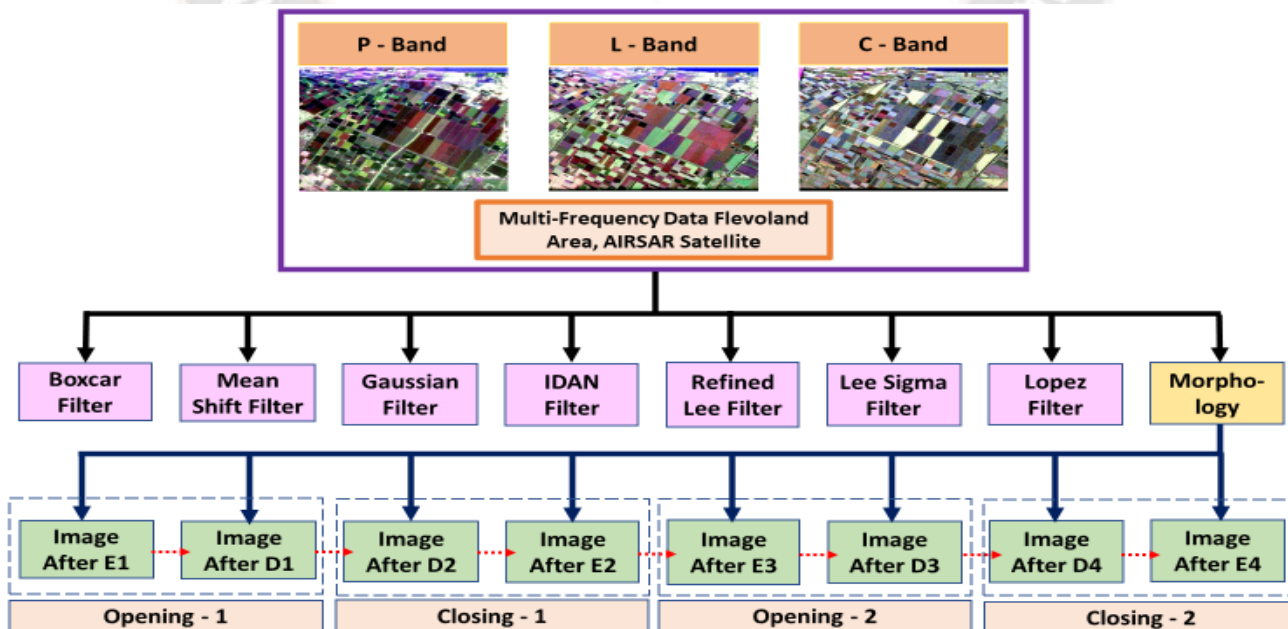


Fig 7: Images generated after applying Morphological and most used filters

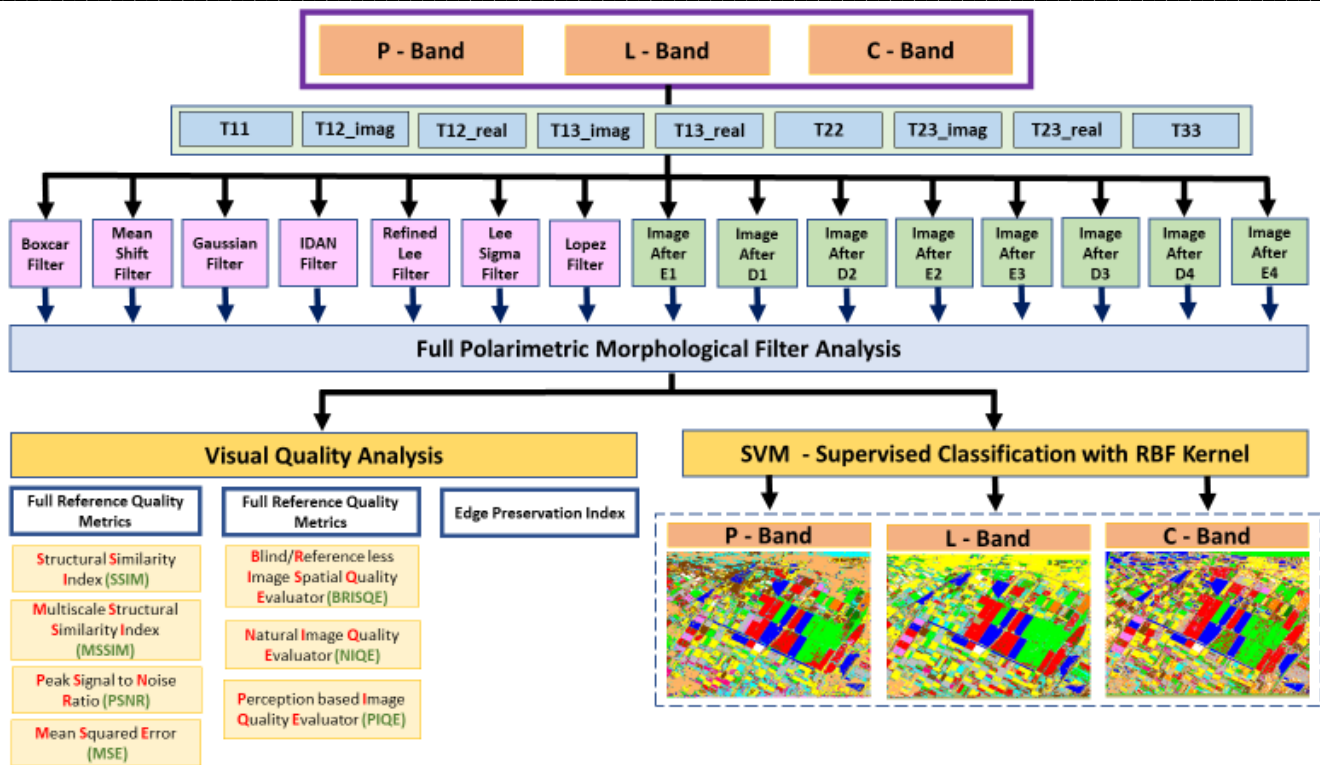


Fig 8: Multi-frequency fully polarimetric morphological filter analysis

Multi-frequency analysis

Morphological Filter and 7 most used filters are applied on each of the P, L and C band PolSAR images. Opening followed by closing is applied twice, while applying morphological operations. The opening and closing operations are carried out sequentially. Each P, L & C band image undergoes two opening and two closing operations. The sequence of these operations is Opening1-Closing1-Opening2-Closing2 (O1-C1-O2-C2). Each Opening and closing operation consist of an erosion and a dilation operation. Hence each P, L, & C image undergoes four erosion and four dilation operations. The Sequence of these operations is Erosion1-Dilation1-Dilation2-Erosion2-Erosion3-Dilation3-Dilation4-Erosion4 (E1-D1-D2-E1-E3-D3-D4-E4). 8 filtered images are generated because of each morphological operation. Hence, we get 15 filtered images for each band of the SAR images. When the above is applied on all the three P, L and C Band images we get a total of 45 filtered images. These 45 filtered images are used for visual quality inspection and classification study.

A. Evaluation of Quality Metrics and Indices

The visual quality of the images is determined using Full reference Quality Metrics, No Reference Quality Metrics and Edge Preservation index. The Full reference Quality Metrics are Mean-squared error (MSE), Peak signal-to-noise ratio (PSNR), Structural Similarity (SSIM) Index & Multi-scale Structural Similarity Index (MSSIM). The No-

reference quality metrics are Blind/Reference less Image Spatial Quality Evaluator (BRISQUE), Natural Image Quality Evaluator (NIQE) and Perception based Image Quality Evaluator (PIQE).

Mean-squared error (MSE): It measures the average squared difference between actual and ideal pixel values. This metric is simple to calculate but might not align well with the human perception of quality.

Peak signal-to-noise ratio (PSNR): It is derived from the mean square error and indicates the ratio of the maximum pixel intensity to the power of the distortion. Like MSE, the PSNR metric is simple to calculate but might not align well with perceived quality.

Structural Similarity Index (SSIM): It combines local image structure, luminance, and contrast into a single local quality score. In this metric, structures are patterns of pixel intensities, especially among neighboring pixels, after normalizing for luminance and contrast. Because the human visual system is good at perceiving structure, the SSIM quality metric agrees more closely with the subjective quality score.

Multi-scale Structural Similarity Index (MSSIM): The MS-SSIM metric expands on the SSIM index by combining luminance information at the highest resolution level with structure and contrast information at several down sampled resolutions, or scales. The multiple scales account for variability in the perception of image details caused by

factors such as viewing distance from the image, distance from the scene to the sensor, and resolution of the image acquisition sensor.

Blind/Reference less Image Spatial Quality Evaluator (BRISQUE): A BRISQUE model is trained on a database of images with known distortions, and BRISQUE is limited to evaluating the quality of images with the same type of distortion. BRISQUE is opinion-aware, which means subjective quality scores accompany the training images.

Natural Image Quality Evaluator (NIQE): Although a NIQE model is trained on a database of pristine images, NIQE can measure the quality of images with arbitrary distortion. NIQE is opinion-unaware and does not use subjective quality scores. The trade-off is that the NIQE score of an image might not correlate as well as the BRISQUE score with human perception of quality.

Perception based Image Quality Evaluator (PIQE): The PIQE algorithm is opinion-unaware and unsupervised, which means it does not require a trained model. PIQE can measure the quality of images with arbitrary distortion and in most cases performs like NIQE. PIQE estimates block-wise distortion and measures the local variance of perceptibly distorted blocks to compute the quality score. Edges in an image determine the visual quality of the image.

Edge Preservation index (EPI): The Edge Preservation Index (EPI) is used to determine the number of edges that are retained after applying the speckle filter. A Laplacian filter is used while calculating the edge preservation index. The parameter alpha controls the shape of the Laplacian and must be in the range 0.0 to 1.0. The value of alpha used is 0.5.

While determining image quality, BRISQUE, NIQE and PIQE scores should be low. SSIM, MSSIM & EPI value should be as high as possible. MSE, SNR and PSNR may not be used as a measure for visual quality since they might not align well with the human perception of quality.

B. Classification study using SVM with RBF Kernel

The quality of filtering is truly incomplete without observing the classification accuracies. Hence a classification study using the Support Vector Machine (SVM) classifier with RBF as the kernel function, was carried out on the filtered images as shown in figure below. 14 Classes were considered during the classification study and accuracy of each class was determined for each of the filtered images. The classification study was carried out for P, L and C Band images to determine the effectiveness of the filter on a particular band of frequency. Same training areas were considered for all the three band images.

TABLE I: CLASS INFORMATION

Class	Name	Color
Class 1	Barley	Red
Class 2	Wheat	Green
Class 3	Rapeseed	Blue
Class 4	Potatoes	Yellow
Class 5	Lucerne	Brown
Class 6	Oats	Dark Green
Class 7	Onions	Cyan
Class 8	Flax	Pink
Class 9	Grass	Brown
Class 10	Beet	Grey
Class 11	Peas	White
Class 12	Beans	Olive
Class 13	Maize	Magenta
Class 14	Fruit	Orange

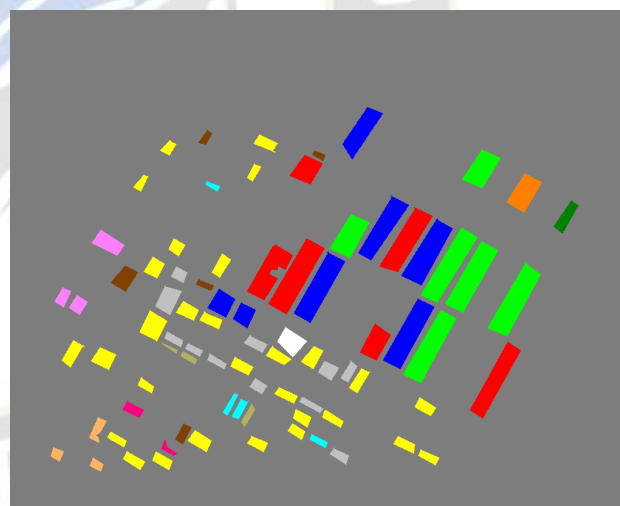


Fig 9: Ground truth information used for giving test areas

TABLE II: QUALITY METRICS FOR P-BAND IMAGES

	T- Matrix Elements	Images obtained after Morphological Operations								Images obtained after most used filters						
		Opening 1		Closing 1		Opening 2		Closing 2		Box	MS	Gau s	IDA N	R Lee	Lee Sig	Lo p
		E1	D1	D2	E2	E3	D3	D4	E4							
BRISQUE SCORE	T11	39.9	35.3	40.7	41.8	44.3	41.9	40.7	41.8	55.68	46.86	51.39	48.46	45.13	57.61	57.11
	T12_ima g	31.8	44.7	55.5	52.9	52.2	53.0	55.5	52.9	56.39	48.56	61.28	53.73	52.49	48.20	47.77
	T12_real	34.3	42.4	51.7	51.3	53.9	51.7	51.7	51.3	56.62	48.67	58.49	56.25	53.88	48.39	56.77
	T13_ima g	45.3	52.7	48.6	48.5	48.7	48.5	48.6	48.5	47.79	45.92	47.45	46.78	47.17	45.92	47.88
	T13_real	49.2	50.9	48.4	48.2	48.7	48.2	48.4	48.2	47.70	45.89	47.58	47.00	47.42	45.99	47.77
	T22	43.9	40.7	44.7	47.5	48.1	47.6	44.7	47.5	55.75	53.80	55.32	49.14	47.25	58.09	56.22
	T23_ima g	49.0	49.1	46.8	47.6	48.5	47.6	46.8	47.6	47.03	45.21	46.55	46.51	45.82	45.48	47.00
	T23_real	55.0	49.2	48.1	48.0	48.8	48.0	48.1	48.0	47.56	45.83	47.26	46.51	46.83	45.87	47.66
	T33	55.1	55.1	52.0	52.9	49.1	52.8	52.0	52.9	54.98	48.89	59.39	51.73	50.60	48.48	55.11
NIQE SCORE	T11	4.5	5.4	5.9	6.7	6.4	6.6	5.9	6.7	5.29	4.73	5.69	5.38	6.32	5.96	5.15
	T12_ima g	5.6	5.5	6.5	7.0	6.5	7.0	6.5	7.0	6.31	6.75	6.11	6.67	6.84	8.28	6.16
	T12_real	5.7	5.7	6.9	7.1	7.3	7.1	6.9	7.1	6.63	7.11	6.43	6.84	7.04	8.57	6.47
	T13_ima g	6.3	6.8	7.5	7.3	7.3	7.3	7.5	7.3	7.04	8.13	7.15	7.99	8.24	10.44	7.04
	T13_real	6.2	7.0	7.7	7.3	7.7	7.3	7.7	7.3	7.50	9.29	7.57	8.33	8.37	10.93	7.50
	T22	4.8	6.2	6.4	7.3	7.4	7.2	6.4	7.3	6.15	5.82	6.09	6.06	6.57	6.69	5.76
	T23_ima g	6.8	8.0	9.2	8.6	8.8	8.6	9.2	8.6	8.91	10.12	9.29	8.76	10.05	11.68	8.91
	T23_real	6.8	7.7	8.4	8.0	8.1	8.0	8.4	8.0	8.10	8.94	8.22	8.76	8.80	10.80	8.10
	T33	7.2	7.7	7.6	8.2	8.6	8.2	7.6	8.2	8.01	7.48	7.78	7.89	8.27	8.79	7.95

PIQUE SCORE	T11	49.7	47.0	59.2	60.7	70.6	60.1	59.2	60.7	76.65	65.06	83.05	63.61	59.22	69.46	81.7
	T12_ima g	50.7	57.8	69.1	61.2	68.8	61.3	69.1	61.2	73.79	67.07	80.04	66.55	57.09	71.26	71.9
	T12_real	47.9	56.7	63.6	59.6	72.4	58.7	63.6	59.6	70.68	70.65	79.63	61.74	55.15	70.40	70.3
	T13_ima g	54.2	64.5	79.4	68.0	74.8	67.0	79.4	68.0	63.70	76.09	77.18	65.45	62.37	70.89	63.7
	T13_real	54.6	65.9	73.7	69.0	78.4	69.3	73.7	69.0	63.84	74.90	63.16	61.59	59.93	71.79	63.8
	T22	56.7	52.8	65.5	65.5	71.3	65.4	65.5	65.5	81.76	69.82	84.70	71.88	65.85	71.34	82.2
	T23_ima g	59.8	71.5	75.0	73.5	74.7	72.8	75.0	73.5	68.55	81.84	67.87	69.27	62.93	77.67	68.5
	T23_real	60.1	69.6	76.4	72.0	77.4	69.6	76.4	72.0	67.98	75.57	77.41	69.27	64.32	75.11	68.0
	T33	65.4	60.5	70.9	72.2	79.7	73.1	70.9	72.2	83.24	76.06	81.24	82.16	73.17	71.06	83.3
SSIM	T11	0.73	0.84	0.78	0.83	0.75	0.83	0.78	0.83	0.78	0.83	0.86	0.81	0.81	0.87	0.78
	T12_ima g	0.70	0.86	0.85	0.85	0.78	0.85	0.85	0.85	0.86	0.86	0.90	0.87	0.87	0.92	0.79
	T12_real	0.66	0.81	0.83	0.82	0.76	0.83	0.83	0.82	0.85	0.85	0.89	0.86	0.86	0.92	0.85
	T13_ima g	0.77	0.88	0.89	0.88	0.84	0.88	0.89	0.88	0.91	0.91	0.93	0.91	0.92	0.96	0.91
	T13_real	0.74	0.85	0.88	0.87	0.82	0.88	0.88	0.87	0.91	0.90	0.93	0.91	0.92	0.96	0.91
	T22	0.79	0.88	0.84	0.88	0.81	0.84	0.84	0.88	0.85	0.89	0.91	0.87	0.86	0.92	0.83
	T23_ima g	0.80	0.89	0.92	0.90	0.87	0.92	0.92	0.90	0.94	0.93	0.95	0.88	0.94	0.97	0.94
	T23_real	0.79	0.89	0.91	0.90	0.85	0.91	0.91	0.90	0.92	0.93	0.95	0.92	0.93	0.97	0.92
	T33	0.89	0.94	0.93	0.94	0.90	0.93	0.93	0.94	0.93	0.94	0.96	0.94	0.93	0.97	0.93
MSSIM	T11	0.79	0.89	0.90	0.89	0.80	0.89	0.90	0.79	0.93	0.94	0.97	0.87	0.89	0.97	0.92
	T12_ima g	0.85	0.95	0.93	0.94	0.91	0.93	0.93	0.85	0.96	0.95	0.98	0.93	0.94	0.98	0.91

EPI	T12_real	0.80	0.90	0.92	0.90	0.86	0.90	0.92	0.80	0.95	0.94	0.98	0.92	0.94	0.98	0.95
	T13_image	0.89	0.96	0.95	0.96	0.94	0.96	0.95	0.89	0.97	0.97	0.99	0.95	0.97	0.99	0.97
	T13_real	0.89	0.95	0.95	0.95	0.94	0.95	0.95	0.89	0.97	0.97	0.99	0.95	0.97	0.99	0.97
	T22	0.84	0.92	0.93	0.92	0.85	0.92	0.93	0.84	0.95	0.96	0.98	0.90	0.92	0.98	0.94
	T23_image	0.91	0.96	0.97	0.97	0.95	0.97	0.97	0.91	0.98	0.98	0.99	0.95	0.98	1.00	0.98
	T23_real	0.90	0.96	0.96	0.96	0.93	0.96	0.96	0.90	0.98	0.98	0.99	0.95	0.97	0.99	0.98
	T33	0.92	0.96	0.97	0.96	0.93	0.96	0.97	0.92	0.97	0.98	0.99	0.95	0.96	0.99	0.97
	T11	0.06	0.63	-0.27	0.63	0.08	0.63	-0.27	0.63	0.93	0.94	0.89	0.94	0.73	0.58	0.93
	T12_image	0.12	0.59	-0.26	0.60	0.14	0.59	-0.26	0.60	0.93	0.94	0.89	0.94	0.68	0.59	0.93
T12_real	0.15	0.21	-0.05	0.24	0.12	0.24	-0.05	0.24	0.81	0.92	0.88	0.89	0.57	0.13	0.81	
T13_image	0.04	0.57	-0.16	0.63	-0.01	0.63	-0.16	0.63	0.91	0.95	0.87	0.94	0.74	0.61	0.91	
T13_real	0.03	0.54	0.09	0.53	-0.19	0.53	0.09	0.53	0.91	0.93	0.86	0.93	0.67	0.46	0.91	
T22	0.15	0.55	-0.25	0.57	0.16	0.55	-0.25	0.57	0.86	0.93	0.87	0.92	0.58	0.53	0.86	
T23_image	0.09	0.32	-0.15	0.40	0.10	0.40	-0.15	0.40	0.86	0.93	0.88	0.94	0.61	0.23	0.86	
T23_real	0.07	0.48	-0.14	0.57	0.03	0.57	-0.14	0.57	0.91	0.94	0.89	0.94	0.66	0.57	0.91	
T33	0.19	0.48	-0.18	0.49	0.19	0.49	-0.18	0.49	0.87	0.92	0.87	0.92	0.54	0.47	0.87	

TABLE III: QUALITY METRICS FOR L-BAND IMAGES

E SCOR	T- Matrix Elements	Images obtained after Morphological Operations								Images obtained after most used filters						
		Opening 1		Closing 1		Opening 2		Closing 2		Box	MS	Gaus	IDAN	R Lee	Lee Sig	Lo p
		E1	D1	D2	E2	E3	D3	D4	E4							
	T11	36.0	36.6	45.2	42.6	49.1	42.4	45.2	42.6	57.98	51.61	49.06	56.01	49.11	47.05	57.6

	T12_ima g	33.4	38.2	50.7	48.8	46.3	48.6	50.7	48.8	51.7	50.0	54.6	48.26	46.9	49.5	47.8
	T12_real	33.7	40.3	49.6	51.4	47.5	51.3	49.6	51.4	54.0	55.7	58.1	52.30	49.5	53.3	54.0
	T13_ima g	35.0	44.4	54.2	46.6	46.3	46.5	54.2	46.6	48.0	46.0	54.9	47.61	48.5	46.3	46.3
	T13_real	34.7	42.3	52.9	48.7	49.1	48.9	52.9	48.7	47.8	46.0	54.1	47.63	48.2	46.4	46.4
	T22	38.3	40.7	49.5	49.4	47.3	49.2	49.5	49.4	61.4	48.3	54.2	56.95	51.6	55.2	55.1
	T23_ima g	38.5	45.7	51.1	46.7	47.5	46.8	51.1	46.7	47.6	45.1	47.8	47.66	47.6	45.9	45.9
	T23_real	40.5	44.3	49.6	50.2	50.2	50.2	49.6	50.2	46.7	45.6	50.3	47.66	47.9	46.1	46.1
	T33	43.7	44.4	48.4	44.0	50.0	44.0	48.4	44.0	51.9	51.7	57.4	47.82	47.3	53.6	52.1
NIQE SCORE	T11	4.11	4.13	5.23	5.44	5.87	5.40	5.23	5.44	4.90	3.91	4.86	4.23	4.37	4.67	4.55
	T12_ima g	5.50	4.53	5.91	6.38	6.29	6.36	5.91	6.38	6.06	6.98	5.51	6.00	5.13	7.45	7.19
	T12_real	4.78	4.02	5.63	5.94	6.21	5.91	5.63	5.94	5.39	6.24	5.22	5.09	4.83	6.19	5.41
	T13_ima g	5.55	5.35	6.89	7.01	7.37	7.01	6.89	7.01	7.13	9.03	6.70	7.93	7.47	9.51	9.51
	T13_real	5.35	5.32	7.18	6.96	7.28	6.94	7.18	6.96	7.17	8.86	6.52	7.65	7.31	9.44	9.44
	T22	3.80	4.31	5.39	5.98	6.51	5.95	5.39	5.98	5.56	4.95	5.29	4.78	4.70	5.24	5.43
	T23_ima g	5.99	5.52	7.62	7.44	7.75	7.44	7.62	7.44	8.78	10.83	7.89	8.92	9.06	10.66	10.66
	T23_real	5.33	5.71	7.74	7.66	7.74	7.65	7.74	7.66	8.25	9.47	7.60	8.92	8.24	10.03	10.00
	T33	5.79	5.98	6.18	6.64	8.01	6.63	6.18	6.64	6.66	6.43	6.39	6.70	6.87	7.33	6.54
PIQUE SCORE	T11	44.3	43.0	61.7	59.2	71.9	58.7	61.7	59.2	74.0	64.3	79.7	67.28	52.9	70.6	71.3
	T12_ima g	47.9	58.4	70.8	63.7	73.2	63.1	70.8	63.7	73.9	72.1	82.6	54.93	49.8	68.5	72.2
	T12_real	48.8	58.3	65.9	66.0	75.5	66.0	65.9	66.0	66.0	69.4	78.9	55.30	50.9	68.7	66.3
	T13_ima g	53.6	68.6	76.6	75.7	76.7	75.8	76.6	75.7	54.8	79.2	78.1	59.23	60.0	72.4	72.4

	T13_real	51.2	63.9	67.2	66.3	78.6	68.1	67.2	66.3	78.14	69.00	74.90	71.49	56.42	73.60	73.6
	T22	52.9	52.0	67.0	65.9	78.4	65.5	67.0	65.9	80.68	71.13	83.23	72.51	59.70	66.58	74.7
	T23_imag	59.4	69.3	81.3	81.7	85.4	81.7	81.3	81.7	94.90	87.82	92.92	78.47	71.08	74.38	74.4
	T23_real	56.7	67.8	79.4	76.5	87.5	79.5	79.4	76.5	90.73	74.63	79.53	78.47	67.71	75.13	75.1
	T33	63.8	59.6	74.6	68.9	81.6	69.3	74.6	68.9	92.99	73.99	80.58	88.56	63.75	66.60	93.0
SSIM	T11	0.71	0.83	0.75	0.81	0.73	0.81	0.75	0.81	0.76	0.78	0.83	0.78	0.77	0.82	0.75
	T12_imag	0.58	0.81	0.85	0.82	0.73	0.82	0.85	0.82	0.89	0.86	0.92	0.89	0.89	0.92	0.80
	T12_real	0.53	0.77	0.84	0.80	0.69	0.80	0.84	0.80	0.87	0.85	0.91	0.88	0.87	0.91	0.87
	T13_imag	0.67	0.84	0.89	0.86	0.80	0.86	0.89	0.86	0.92	0.91	0.94	0.93	0.93	0.95	0.95
	T13_real	0.67	0.83	0.89	0.86	0.79	0.86	0.89	0.86	0.92	0.92	0.95	0.93	0.93	0.95	0.95
	T22	0.81	0.89	0.85	0.88	0.83	0.88	0.85	0.88	0.86	0.88	0.91	0.88	0.87	0.90	0.84
	T23_imag	0.75	0.89	0.93	0.91	0.86	0.91	0.93	0.91	0.96	0.95	0.97	0.90	0.96	0.97	0.97
	T23_real	0.75	0.88	0.93	0.90	0.85	0.90	0.93	0.90	0.95	0.94	0.97	0.95	0.95	0.97	0.97
	T33	0.88	0.95	0.92	0.94	0.90	0.94	0.92	0.94	0.93	0.94	0.96	0.94	0.93	0.96	0.93
MSSSIM	T11	0.86	0.91	0.90	0.91	0.86	0.91	0.90	0.91	0.93	0.92	0.97	0.91	0.91	0.95	0.92
	T12_imag	0.90	0.97	0.96	0.97	0.95	0.97	0.96	0.97	0.97	0.96	0.99	0.96	0.97	0.99	0.96
	T12_real	0.86	0.94	0.95	0.94	0.92	0.94	0.95	0.94	0.97	0.96	0.98	0.96	0.96	0.98	0.97
	T13_imag	0.92	0.97	0.97	0.97	0.96	0.97	0.97	0.97	0.98	0.98	0.99	0.98	0.98	0.99	0.99
	T13_real	0.92	0.97	0.97	0.97	0.95	0.97	0.97	0.97	0.98	0.98	0.99	0.97	0.98	0.99	0.99
	T22	0.92	0.95	0.94	0.95	0.92	0.95	0.94	0.95	0.96	0.96	0.98	0.95	0.95	0.98	0.95
	T23_imag	0.96	0.98	0.99	0.99	0.98	0.99	0.99	0.99	0.99	0.99	1.00	0.98	0.99	1.00	1.00

	T23_real	0.95	0.98	0.98	0.98	0.97	0.98	0.98	0.98	0.99	0.99	0.99	0.98	0.99	1.00	1.00
	T33	0.96	0.98	0.98	0.98	0.96	0.98	0.98	0.98	0.98	0.98	0.99	0.98	0.97	0.99	0.98
EPI	T11	0.14	0.44	-0.12	0.45	0.12	0.45	-0.12	0.45	0.87	0.89	0.88	0.92	0.60	0.30	0.85
	T12_ima g	0.10	0.35	0.14	0.35	-0.07	0.35	0.14	0.35	0.83	0.90	0.87	0.89	0.55	0.27	0.83
	T12_real	0.10	0.25	-0.02	0.27	0.14	0.27	-0.02	0.27	0.82	0.64	0.85	0.87	0.52	0.28	0.80
	T13_ima g	0.09	0.25	0.16	0.15	0.00	0.15	0.16	0.15	0.76	0.66	0.84	0.82	0.36	0.18	0.18
	T13_real	0.07	0.29	-0.04	0.30	0.13	0.30	-0.04	0.30	0.83	0.82	0.86	0.88	0.52	0.25	0.25
	T22	0.19	0.33	-0.06	0.34	0.19	0.34	-0.06	0.34	0.87	0.53	0.87	0.89	0.41	0.39	0.77
	T23_ima g	0.13	0.13	0.03	0.16	0.16	0.15	0.03	0.16	0.75	0.77	0.85	0.83	0.43	0.17	0.17
	T23_real	0.07	0.10	-0.02	0.23	0.18	0.23	-0.02	0.23	0.80	0.57	0.85	0.83	0.39	0.32	0.32
	T33	0.15	0.37	-0.06	0.38	0.13	0.38	-0.06	0.38	0.83	0.63	0.86	0.89	0.43	0.32	0.81

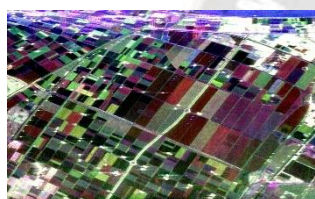
TABLE IV: QUALITY METRICS FOR C-BAND IMAGES

	T-Matrix Elements	Images obtained after Morphological Operations								Images obtained after most used filters						
		Opening 1		Closing 1		Opening 2		Closing 2		Bo x	MS	Gaus	IDAN	R Lee	Lee Sig	Lo p
		E1	D1	D2	E2	E3	D3	D4	E4							
BRISQ SCORE	T11	39.1	22.1	38.2	43.5	44.4	43.5	38.2	43.5	55.0	35.0	48.6	52.6	46.2	46.2	55.0
	T12_ima g	42.6	26.6	38.2	39.8	49.4	39.6	38.2	39.8	49.5	50.9	47.3	47.7	33.5	33.5	49.5
	T12_real	41.6	26.5	34.5	40.4	48.6	40.3	34.5	40.4	50.5	52.7	47.9	50.3	35.5	35.5	50.5
	T13_ima g	37.6	30.2	40.5	37.5	44.7	36.8	40.5	37.5	46.9	54.5	48.0	46.8	28.1	28.1	46.9
	T13_real	37.6	30.7	40.2	37.2	47.0	36.4	40.2	37.2	49.0	57.1	49.0	47.8	28.5	28.5	49.0
	T22	28.1	26.7	44.7	41.1	50.1	41.1	44.7	41.1	53.8	43.8	44.7	51.5	44.6	44.6	53.8
	T23_ima	22.5	26.	45.3	36.6	49.5	37.0	45.3	36.6	52.	48.0	45.9	53.6	35.4	35.4	52.

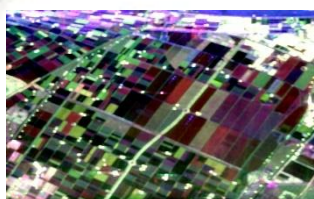
	g		0							2						2
	T23_real	23.7	24.7	44.6	36.7	50.2	37.2	44.6	36.7	51.8	48.5	45.9	53.6	35.2	35.2	53.8
	T33	23.1	25.8	40.5	37.5	44.3	37.2	40.5	37.5	57.1	44.5	45.8	53.3	47.8	47.8	57.1
NIQE SCORE	T11	6.65	5.80	8.09	8.87	6.52	8.78	8.09	8.87	4.89	3.29	5.64	3.94	3.95	3.95	4.89
	T12_imag	7.77	6.62	6.78	8.30	5.83	8.15	6.78	8.30	4.66	5.21	4.98	3.94	2.86	2.86	4.66
	T12_real	7.69	6.27	6.88	8.04	6.17	7.94	6.88	8.04	4.40	4.44	5.12	3.94	2.99	2.99	4.40
	T13_imag	7.87	6.45	6.77	7.81	6.43	7.73	6.77	7.81	4.93	7.38	5.27	4.42	3.20	3.20	4.93
	T13_real	7.23	6.22	6.54	7.27	6.12	7.17	6.54	7.27	4.76	6.52	5.13	4.23	3.28	3.28	4.76
	T22	5.57	5.07	6.12	7.35	6.18	7.27	6.12	7.35	5.00	3.77	5.02	4.00	3.73	3.73	5.00
	T23_imag	6.67	5.75	6.34	6.59	6.20	6.54	6.34	6.59	5.84	9.49	5.35	5.18	3.87	3.87	5.84
	T23_real	6.66	5.56	6.06	6.59	6.21	6.48	6.06	6.59	5.76	7.94	5.32	5.18	3.72	3.72	5.76
	T33	4.60	4.33	5.25	6.18	6.06	6.11	5.25	6.18	5.14	4.03	4.80	4.33	3.95	3.95	5.14
PIQUE SCORE	T11	19.6	19.2	40.3	42.1	58.0	42.6	40.3	42.1	58.3	56.2	65.6	51.0	30.1	30.1	58.3
	T12_imag	18.6	32.8	62.0	56.0	70.7	55.7	62.0	56.0	35.9	79.7	51.6	34.1	22.7	22.7	35.9
	T12_real	16.9	27.7	59.5	54.3	70.4	54.6	59.5	54.3	40.6	74.9	57.3	34.3	24.3	24.3	40.6
	T13_imag	20.0	35.5	64.6	58.8	73.9	59.0	64.6	58.8	33.4	85.4	51.3	32.0	26.1	26.1	33.4
	T13_real	20.1	36.8	66.4	59.3	72.7	58.6	66.4	59.3	38.8	80.4	51.3	38.3	29.0	29.0	38.8
	T22	25.9	26.7	54.9	52.7	70.3	53.2	54.9	52.7	62.1	63.8	68.1	58.3	38.7	38.7	62.1
	T23_imag	27.4	44.7	70.5	63.5	77.5	62.8	70.5	63.5	33.2	71.6	47.0	38.8	37.8	37.8	33.2
	T23_real	28.9	45.7	72.3	63.6	79.2	63.4	72.3	63.6	42.5	80.4	53.3	38.8	39.0	39.0	42.5
	T33	36.9	37.0	60.5	58.0	71.7	57.6	60.5	58.0	60.4	66.8	71.9	66.6	45.2	45.2	60.4

SSIM	T11	0.39	0.58	0.33	0.48	0.34	0.48	0.33	0.48	0.33	0.35	0.50	0.36	0.36	0.36	0.33
	T12_imag	-0.02	0.25	0.40	0.30	0.14	0.30	0.40	0.30	0.51	0.46	0.62	0.52	0.52	0.52	0.51
	T12_real	0.06	0.28	0.40	0.32	0.18	0.32	0.40	0.32	0.51	0.45	0.63	0.51	0.52	0.52	0.51
	T13_imag	0.09	0.27	0.42	0.32	0.20	0.32	0.42	0.32	0.57	0.52	0.67	0.57	0.58	0.58	0.57
	T13_real	0.11	0.32	0.44	0.35	0.22	0.35	0.44	0.35	0.57	0.52	0.67	0.57	0.58	0.58	0.57
	T22	0.57	0.71	0.57	0.66	0.57	0.66	0.57	0.66	0.58	0.59	0.69	0.59	0.59	0.59	0.59
	T23_imag	0.21	0.44	0.59	0.49	0.37	0.49	0.59	0.49	0.73	0.69	0.80	0.61	0.74	0.74	0.73
	T23_real	0.16	0.40	0.59	0.47	0.33	0.47	0.59	0.47	0.73	0.68	0.79	0.72	0.73	0.73	0.73
	T33	0.66	0.79	0.67	0.75	0.67	0.75	0.67	0.75	0.69	0.70	0.77	0.70	0.70	0.70	0.70
MSSIM	T11	0.74	0.83	0.75	0.80	0.72	0.80	0.75	0.80	0.79	0.73	0.90	0.77	0.78	0.78	0.79
	T12_imag	0.00	0.76	0.81	0.78	0.67	0.78	0.81	0.78	0.87	0.82	0.92	0.84	0.86	0.86	0.87
	T12_real	0.00	0.79	0.80	0.79	0.71	0.79	0.80	0.79	0.86	0.81	0.93	0.83	0.85	0.85	0.86
	T13_imag	0.64	0.80	0.83	0.80	0.75	0.80	0.83	0.80	0.89	0.86	0.93	0.88	0.89	0.89	0.89
	T13_real	0.72	0.85	0.84	0.83	0.79	0.83	0.84	0.83	0.89	0.86	0.94	0.88	0.89	0.89	0.89
	T22	0.80	0.86	0.83	0.85	0.80	0.85	0.83	0.85	0.87	0.84	0.94	0.84	0.86	0.86	0.87
	T23_imag	0.80	0.90	0.91	0.90	0.87	0.90	0.91	0.90	0.94	0.93	0.97	0.90	0.94	0.94	0.94
	T23_real	0.73	0.87	0.89	0.87	0.83	0.87	0.89	0.87	0.94	0.92	0.96	0.92	0.93	0.93	0.94
	T33	0.88	0.93	0.90	0.92	0.88	0.92	0.90	0.92	0.94	0.89	0.96	0.91	0.91	0.91	0.92
EPI	T11	0.05	0.19	-0.05	0.18	0.04	0.18	-0.05	0.18	0.09	0.18	0.86	0.39	0.49	0.49	0.43
	T12_imag	-0.01	0.14	0.12	0.05	0.01	0.05	0.12	0.05	0.40	0.35	0.86	-0.73	0.34	0.34	0.40

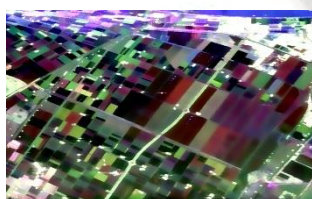
T12_real	0.04	0.09	-0.02	0.10	0.13	0.10	-0.02	0.10	0.80	0.16	0.87	0.62	0.51	0.51	0.80
T13_imag	0.05	0.19	0.12	0.06	0.08	0.06	0.12	0.06	0.72	0.07	0.87	0.03	0.40	0.40	0.72
T13_real	0.00	0.52	0.09	0.03	0.01	0.03	0.09	0.03	0.79	0.05	0.88	0.23	0.51	0.51	0.79
T22	0.14	0.52	0.01	0.50	0.14	0.50	0.01	0.50	0.83	0.52	0.87	0.75	0.33	0.33	0.83
T23_imag	0.01	0.04	0.04	0.02	0.03	0.02	0.04	0.02	0.04	0.12	0.86	-0.65	0.09	0.09	0.04
T23_real	-0.02	0.26	0.08	-0.05	-0.01	-0.05	0.08	-0.05	0.74	-0.45	0.89	-0.65	0.40	0.40	0.74
T33	0.14	0.25	-0.05	0.28	0.11	0.28	-0.05	0.28	0.80	0.45	0.88	0.59	0.36	0.36	0.81



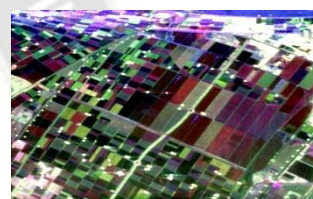
(a) Original



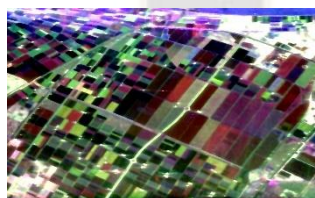
(b) Boxcar



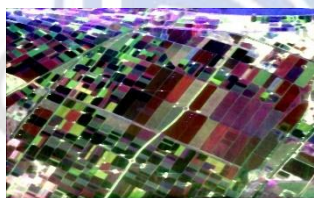
(c) Mean Shift



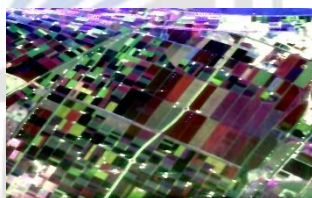
(d) Gaussian



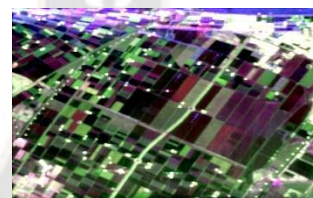
(e) IDAN Filter



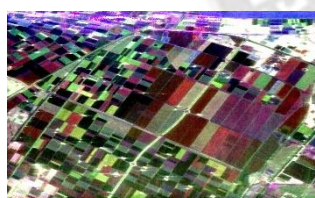
(f) Refined Lee Filter



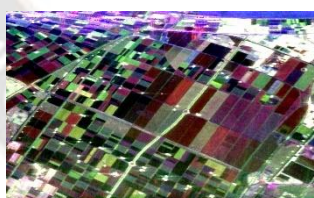
(g) Lee Sigma Filter



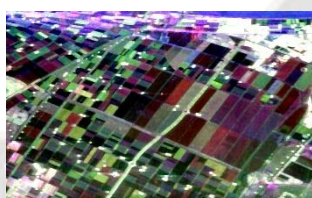
(h) Lopez Filter



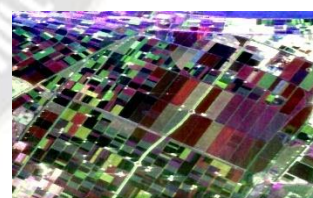
(i) Image After Erosion 1



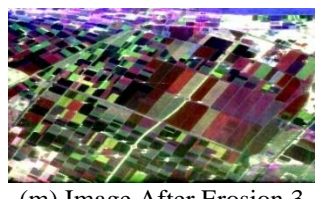
(j) Image After Dilation 1



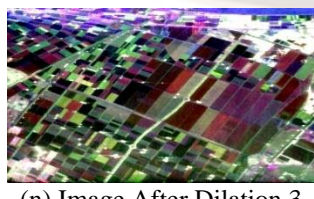
(k) Image After Dilation 2



(l) Image After Erosion 2



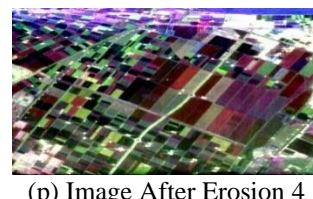
(m) Image After Erosion 3



(n) Image After Dilation 3



(o) Image After Dilation 4



(p) Image After Erosion 4

Fig 10: Pauli RGB of original and filtered images with P-Band PolSAR Images

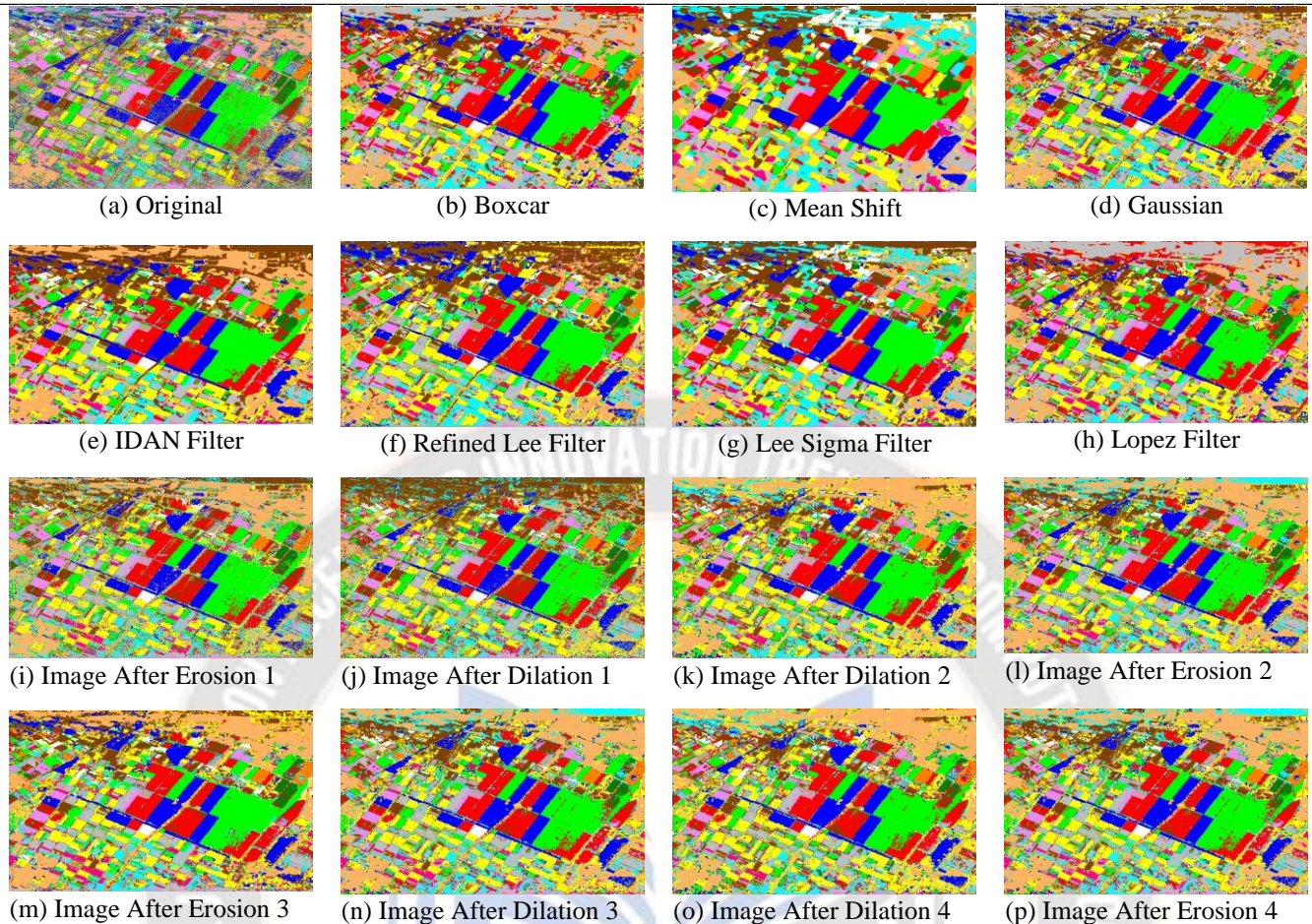


Fig 11: Classification results with P-Band PolSAR Images

TABLE V: CLASSIFICATION ACCURACY FOR P-BAND IMAGES USING MOST USED FILTERS

Class	Name	Color	Original	Boxcar	Mean Shift	Gaussian	IDAN	Refined Lee	Lopez	Lee Sigma
1	Barley	Red	78.62	98.73	99.83	98.33	99.73	99.31	97.81	99.24
2	Wheat	Green	94.05	99.78	99.97	99.46	99.92	99.75	99.58	99.89
3	Rapeseed	Blue	89.12	99.93	100.00	99.94	99.98	99.93	99.87	99.98
4	Potatoes	Yellow	78.01	98.38	99.07	98.02	99.17	98.85	97.54	96.54
5	Lucerne	Brown	96.08	99.93	100.00	100.00	99.93	100.00	99.86	99.86
6	Oats	Dark Green	86.68	100.00	100.00	100.00	100.00	100.00	100.00	100.00
7	Onions	Cyan	43.72	94.83	97.57	83.32	95.35	83.21	89.97	90.71
8	Flax	Pink	79.80	97.07	98.63	96.23	96.47	96.71	96.23	97.55
9	Grass	Brown	60.52	98.87	99.29	96.73	99.70	96.97	97.80	96.31
10	Beet	Grey	55.99	81.36	77.80	76.64	82.93	83.66	76.86	80.20
11	Peas	White	95.74	99.69	100.00	99.79	100.00	100.00	99.48	100.00
12	Beans	Olive	34.51	94.37	97.36	85.74	96.65	87.68	79.05	94.89

13	Maize		77.78	99.45	99.64	98.72	100.00	99.82	98.36	99.64
14	Fruit		97.40	100.00	100.00	100.00	100.00	99.77	100.00	100.00

TABLE VI: CLASSIFICATION ACCURACY FOR P-BAND IMAGES USING MORPHOLOGICAL FILTERS

Class	Name	Color	Original	Erosion 1	Dilation 1	Dilation 2	Erosion 2	Erosion 3	Dilation 3	Dilation 4	Erosion 4
1	Barley		78.62	91.49	93.03	96.49	97.90	98.56	97.80	96.49	97.90
2	Wheat		94.05	98.73	98.54	99.26	99.13	99.61	99.16	99.26	99.13
3	Rapeseed		89.12	97.54	98.26	99.86	99.87	99.99	99.87	99.86	99.87
4	Potatoes		78.01	93.83	95.87	97.28	97.57	97.12	97.51	97.28	97.57
5	Lucerne		96.08	99.39	99.46	99.46	99.86	100.00	99.80	99.46	99.86
6	Oats		86.68	96.63	97.22	98.39	98.83	99.85	98.83	98.39	98.83
7	Onions		43.72	66.42	69.38	81.84	80.89	87.65	81.31	81.84	80.89
8	Flax		79.80	87.69	87.63	88.94	92.17	95.70	92.59	88.94	92.17
9	Grass		60.52	89.66	92.63	96.25	97.03	95.90	96.97	96.25	97.03
10	Beet		55.99	62.01	68.97	74.67	74.72	78.16	74.77	74.67	74.72
11	Peas		95.74	98.13	98.54	99.69	99.58	99.48	99.58	99.69	99.58
12	Beans		34.51	61.27	72.54	88.20	84.33	83.98	84.33	88.20	84.33
13	Maize		77.78	90.89	96.17	96.17	96.36	98.36	96.72	96.17	96.36
14	Fruit		97.40	99.10	98.42	99.77	100.00	100.00	100.00	99.77	100.00



(a) Original



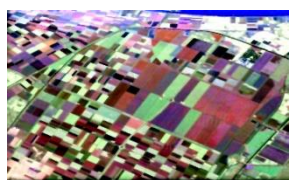
(b) Boxcar



(c) Mean Shift



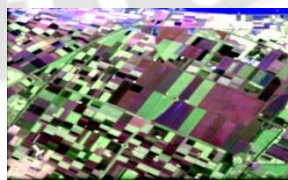
(d) Gaussian



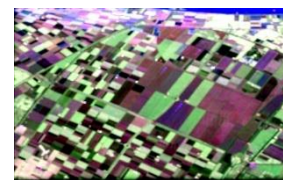
(e) IDAN Filter



(f) Refined Lee Filter



(g) Lee Sigma Filter



(h) Lopez Filter



(i) Image After Erosion 1



(j) Image After Dilation 1



(k) Image After Dilation 2



(l) Image After Erosion 2

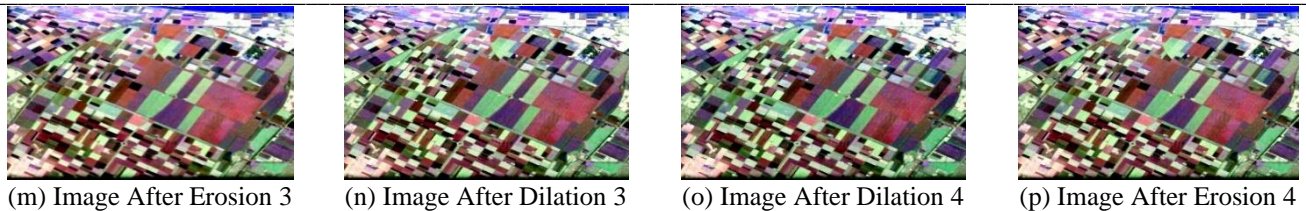


Fig 12: Pauli RGB of original and filtered images with L-Band PolSAR Images

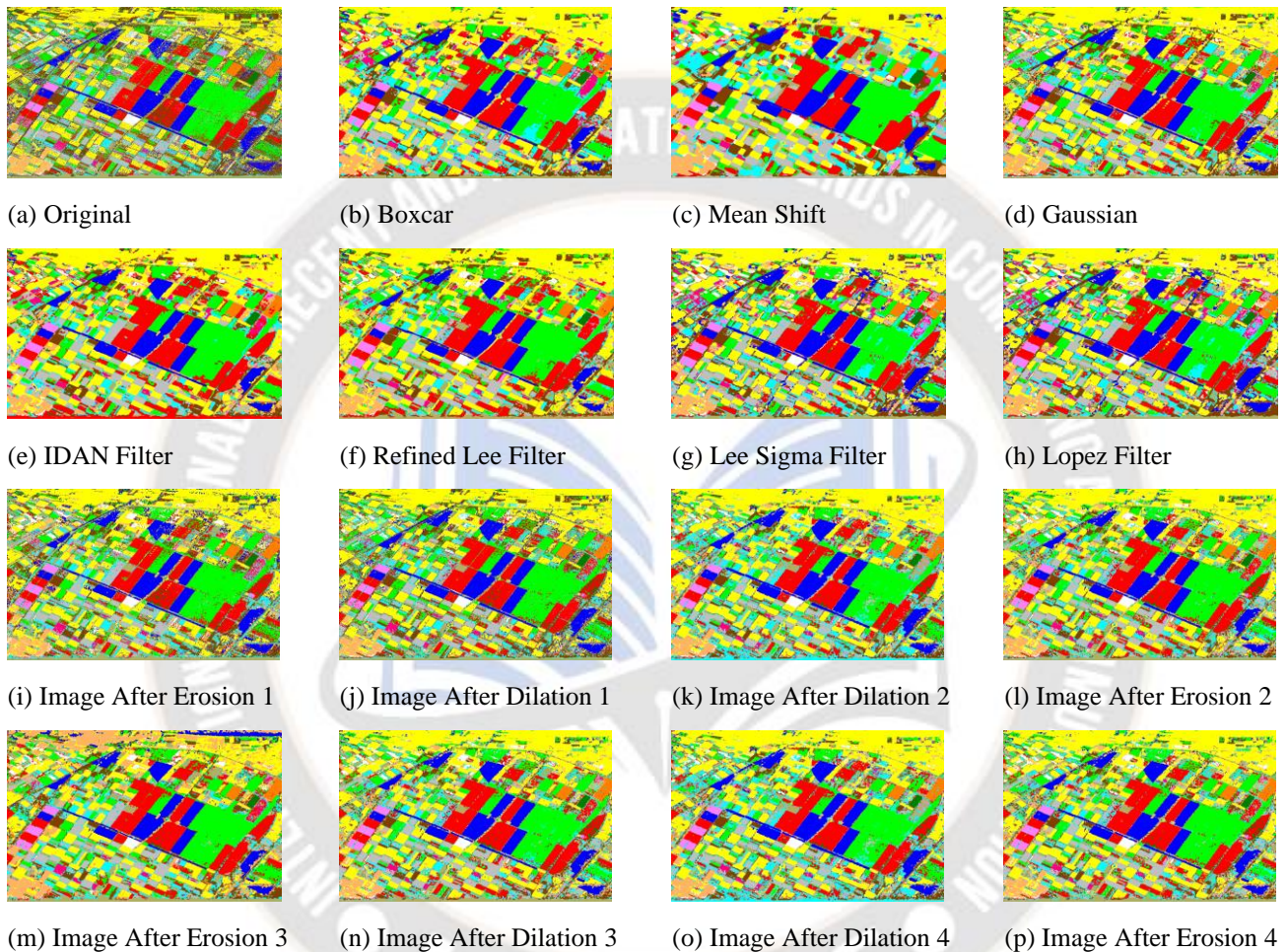


Fig 13: Classification results with L-Band PolSAR Images

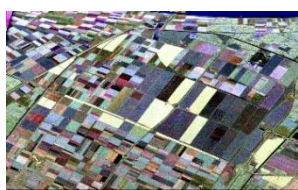
TABLE VII: CLASSIFICATION ACCURACY FOR L-BAND IMAGES USING MOST USED FILTERS

Class	Name	Color	Original	Boxcar	Mean Shift	Gaussian	IDAN	Refined Lee	Lopez	Lee Sigma
1	Barley	Red	89.90	99.98	99.96	99.92	99.92	99.86	99.89	99.96
2	Wheat	Green	93.99	99.26	99.83	99.52	99.57	99.94	98.72	99.56
3	Rapeseed	Blue	92.37	100.00	100.00	100.00	100.00	99.95	99.99	100.00
4	Potatoes	Yellow	88.16	99.83	99.76	99.13	99.86	99.56	99.60	99.92
5	Lucerne	Brown	97.09	99.86	100.00	99.80	99.86	99.93	99.80	99.93
6	Oats	Dark Green	96.63	100.00	100.00	100.00	100.00	100.00	100.00	100.00

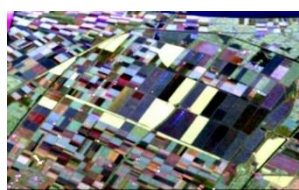
7	Onions		77.30	99.58	99.79	99.47	99.79	99.47	98.94	99.79
8	Flax		98.92	100.00	100.00	100.00	99.94	99.94	100.00	99.94
9	Grass		92.39	99.88	100.00	99.88	99.94	100.00	99.82	100.00
10	Beet		78.35	98.65	99.64	98.72	99.24	99.41	98.06	99.12
11	Peas		97.82	99.58	100.00	99.58	99.79	100.00	99.48	100.00
12	Beans		87.32	99.82	100.00	99.47	99.65	100.00	99.12	99.82
13	Maize		83.24	100.00	100.00	100.00	100.00	100.00	99.45	100.00
14	Fruit		88.24	99.89	100.00	99.77	99.77	99.43	100.00	99.10

TABLE VIII: CLASSIFICATION ACCURACY FOR L-BAND IMAGES USING MORPHOLOGICAL FILTERS

Class	Name	Color	Original	Erosion 1	Dilation 1	Dilation 2	Erosion 2	Erosion 3	Dilation 3	Dilation 4	Erosion 4
1	Barley		89.90	95.42	96.91	98.77	98.64	99.37	98.62	98.77	98.64
2	Wheat		93.99	98.23	97.97	97.97	99.01	99.84	98.28	97.97	99.01
3	Rapeseed		92.37	98.35	99.02	99.96	99.94	99.98	99.94	99.96	99.94
4	Potatoes		88.16	95.65	97.58	99.10	98.99	98.72	98.94	99.10	98.99
5	Lucerne		97.09	99.53	100.00	100.00	99.93	99.86	99.93	100.00	99.93
6	Oats		96.63	99.41	99.41	99.85	100.00	99.85	100.00	99.85	100.00
7	Onions		77.30	93.77	94.19	97.57	98.63	99.26	98.73	97.57	98.63
8	Flax		98.92	99.76	99.64	99.76	100.00	99.88	100.00	99.76	100.00
9	Grass		92.39	97.68	97.86	99.05	99.05	99.46	98.87	99.05	99.05
10	Beet		78.35	91.13	93.08	95.66	97.91	97.96	97.84	95.66	97.91
11	Peas		97.82	99.90	99.38	100.00	99.90	99.79	99.90	100.00	99.90
12	Beans		87.32	96.30	98.24	98.59	99.47	98.94	99.30	98.59	99.47
13	Maize		83.24	98.18	98.36	98.00	99.82	100.00	99.82	98.00	99.82
14	Fruit		88.24	96.95	97.51	99.77	98.98	98.30	99.10	99.77	98.98



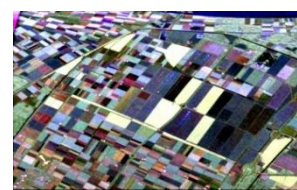
(a) Original



(b) Boxcar



(c) Mean Shift



(d) Gaussian

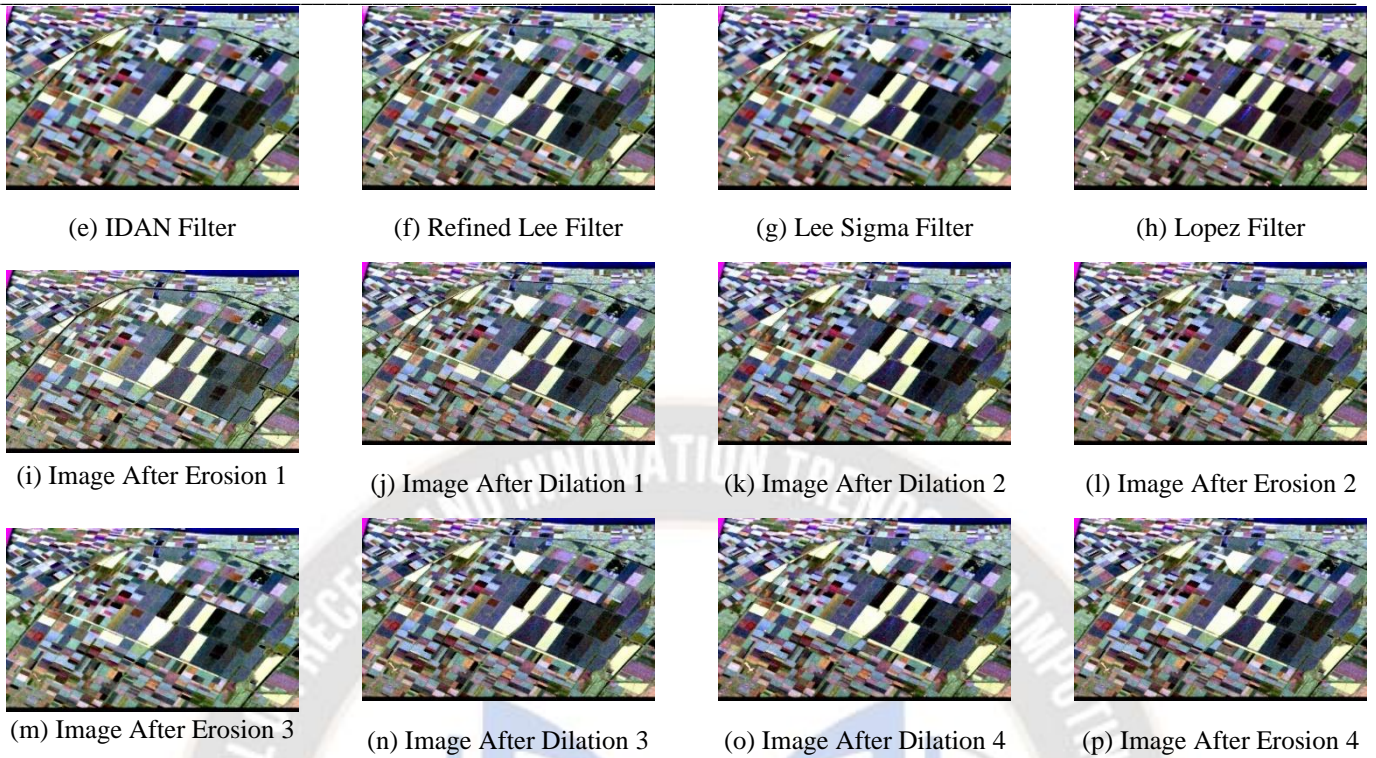


Fig 14: Pauli RGB of original and filtered images with C-Band PolSAR Images

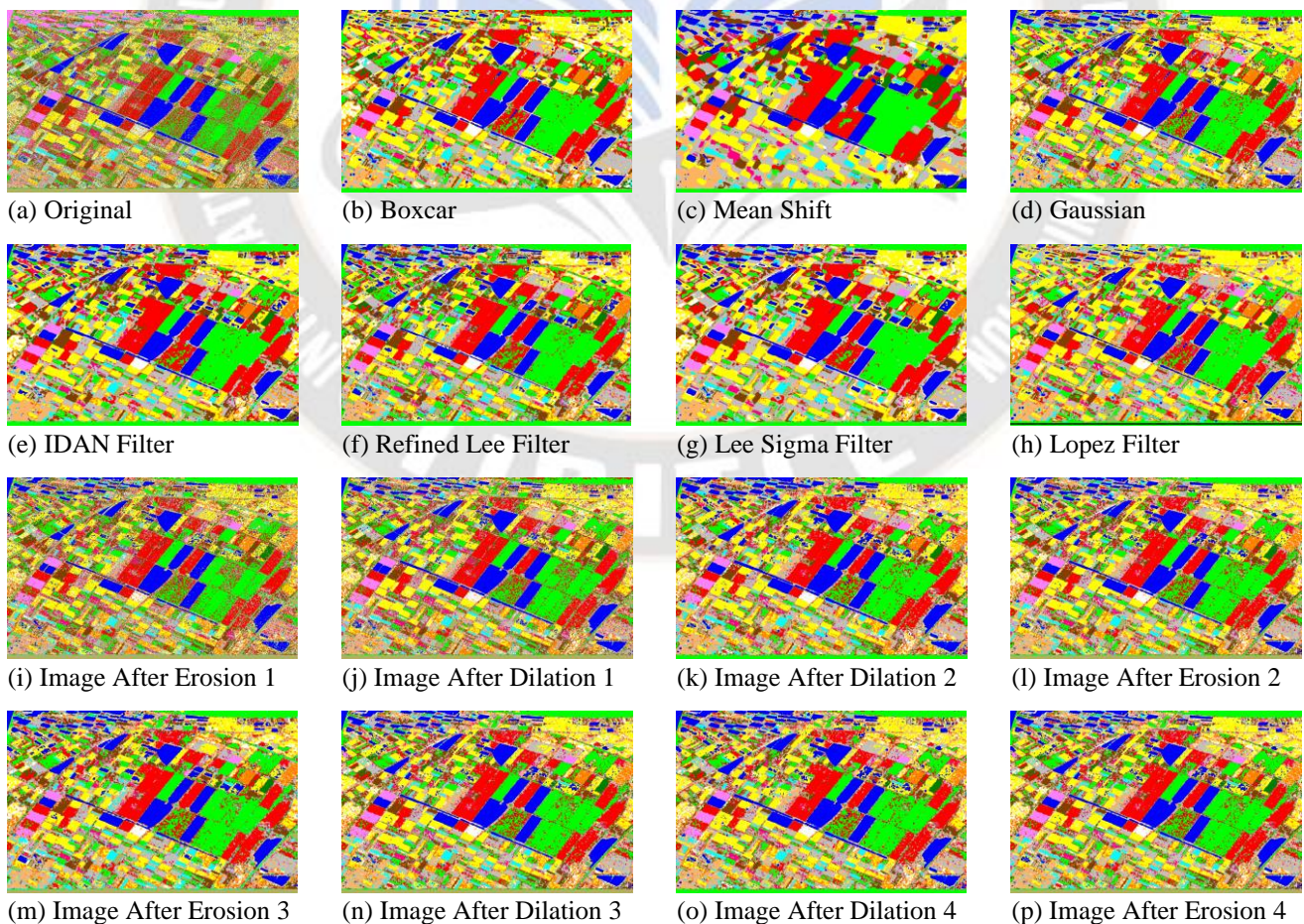


Fig 15: Classification results with C-Band PolSAR Images

TABLE XI: CLASSIFICATION ACCURACY FOR C-BAND IMAGES USING MOST USED FILTERS

Class	Name	Color	Original	Boxcar	Mean Shift	Gaussian	IDAN	Refined Lee	Lopez	Lee Sigma
1	Barley		59.33	97.04	99.95	93.74	97.53	95.67	91.89	98.88
2	Wheat		80.16	97.16	99.78	95.50	98.12	96.98	96.41	98.27
3	Rapeseed		96.96	99.99	100.00	100.00	100.00	99.96	99.99	100.00
4	Potatoes		53.76	93.70	99.60	89.94	92.82	90.04	88.90	95.16
5	Lucerne		47.67	99.59	100.00	96.15	98.85	96.82	95.40	99.05
6	Oats		70.86	100.00	100.00	100.00	100.00	99.85	100.00	100.00
7	Onions		81.84	100.00	100.00	99.79	99.68	97.78	99.37	99.58
8	Flax		88.34	100.00	100.00	99.88	100.00	99.94	100.00	100.00
9	Grass		73.66	99.29	100.00	99.29	99.64	99.70	99.35	99.94
10	Beet		30.42	94.88	99.95	88.26	95.90	90.44	86.44	99.08
11	Peas		57.07	99.79	100.00	99.48	99.79	99.79	97.09	99.90
12	Beans		97.01	99.82	100.00	100.00	100.00	100.00	99.82	100.00
13	Maize		54.10	99.09	100.00	97.09	99.45	95.08	96.36	99.64
14	Fruit		34.50	98.08	100.00	98.30	99.55	96.49	96.83	99.77

TABLE X: CLASSIFICATION ACCURACY FOR C-BAND IMAGES USING MORPHOLOGICAL FILTERS

Class	Name	Color	Original	Erosion 1	Dilation 1	Dilation 2	Erosion 2	Erosion 3	Dilation 3	Dilation 4	Erosion 4
1	Barley		59.33	75.59	81.15	89.42	89.75	92.45	89.92	89.42	89.75
2	Wheat		80.16	88.98	90.28	93.09	93.11	94.29	93.19	93.09	93.11
3	Rapeseed		96.96	98.91	99.88	100	100	99.99	100	100	100
4	Potatoes		53.76	68.73	74.77	84.42	83.92	85.29	84.05	84.42	83.2
5	Lucerne		47.67	74.98	80.93	93.31	92.49	94.79	92.29	93.31	92.49
6	Oats		70.86	91.8	93.56	99.56	99.27	99.85	99.27	99.56	99.27
7	Onions		81.84	88.28	93.14	98.42	98.63	97.25	99.05	98.42	98.63
8	Flax		88.34	97.13	98.63	99.88	99.82	100	99.82	99.88	99.82

9	Grass		73.66	86.03	88.41	94.59	95.96	98.22	95.96	94.59	95.96
10	Beet		30.42	56.51	61.58	78.73	77.42	86.74	78.09	78.73	77.42
11	Peas		57.07	75.36	84.51	96.36	95.22	96.78	95.32	96.36	95.22
12	Beans		97.01	98.06	97.18	97.89	99.47	99.65	99.47	97.89	99.47
13	Maize		54.1	81.24	81.97	90.89	90.89	93.99	90.35	90.89	90.89
14	Fruit		34.5	65.38	72.62	90.84	89.03	90.27	89.93	90.84	89.03

V. RESULTS

The fully polarimetric speckle filtering is carried out applying consecutive opening & closing operations, twice on every image to assess the effect of idempotent nature of morphological operations on visual quality and classification accuracies. The sequence of applying the morphological operation is O-C-O-C, where ‘O’ stands for opening & ‘C’ stands for closing. Each Opening and closing operation are based on Erosion and dilation operation. Hence the sequence of applying the morphological operation in terms of Erosion and Dilation is ‘E-D-D-E-E-D-D-E’, where ‘E’ stands for erosion and ‘D’ stands for dilation.

The performance of the fully polarimetric speckle filter based on morphological operations is determined by analyzing the visual quality of the followed by a classification study at multiple frequencies. The visual quality indices used are BRISQE, NIQE, PIQE, SSIM, MSSSIM, and EPI. The visual quality metrics are calculated for each element of the T-Matrix for the filtered images as shown in fig.7 & fig 8. Quality metrics of images obtained after each Morphological operation are compared with the most used speckle filters like Boxcar (Box), Mean shift (MS), Gaussian (Gaus), IDAN, Refined Lee (R Lee), Lee Sigma (Lee Sig) and Lopez (Lop). The values of the above quality metrics are determined for the P, L & C bands PolSAR images. This is as shown in Table II, III and IV. It can be noted that quality metrics obtained after the second opening and closing operations, i.e. after erosion 4 (E4) are similar to the first opening and closing operations, i.e. after Erosion 2 (E2), at all frequencies. This is due to the idempotent nature of morphological operations. For analysis purpose T11, T22 and T33 components of the T-Matrix are considered. For P & L-Band PolSAR images the BRISQE, NIQE scores PIQE are low for the morphological filter as compared to other filters. SSIM and MSSSIM values are high and nearly equal to that of other filters. The Edge preservation index is nearly equal to the Lee Sigma filtered images;

however, it is lower as compared to other filters. This is as shown in table II and III. For C-Band PolSAR images the BRISQE and PIQE scores are low, however NIQE SCORES are comparatively higher, for the morphological filter as compared to other filters. SSIM and MSSSIM values are high and nearly equal to that of other filters. The Edge preservation index is lower as compared to other filters. This is as shown in table IV. Pauli RGB images for original and the filtered images are generated for visual inspection as shown in fig. (10,12 and 14).

The calculation of the visual quality indices is followed by a classification study using the Support Vector Machine classifier for all the three P, L& C band images.14 different classes are considered in the classification study as listed in Table I. Since the number of classes are high, RBF (Radial Basis Function) is used as the kernel function. Cross validation is carried out before determining actual class accuracies. The ground truth data used for training the SVM classifier is as shown in fig. 9. The classification results after applying the fully polarimetric morphological filter for P, L & C bands is as shown in fig. (11,13, and 15) respectively. Each figure consists of classified images after applying the SVM Classifier on the Original, as well as filtered images. The fig. (11,13, and 15)also consists of classified images after every morphological operation.

The classification accuracies for each of the filtered images using P-Band PolSAR image is as shown in table V and VI, for L-BandPolSAR image is as shown in table VII and VIII and C-Band PolSAR images is as shown in table XI and X. It can be noted that the classification accuracy values obtained for each class after the second opening and closing operations, i.e after Erosion 4 (E4) are similar to the first opening and closing operations, i.e after Erosion 2 (E2), at all frequencies. This is again due to the idempotent nature of morphological operations.

It can be observed that the classification accuracies obtained for each class after applying the fully polarimetric morphological filter are high and comparable with the Boxcar Filter, Mean Shift Filter, Gaussian Filter, IDAN Filter, Refined Lee Filter, Lee Sigma Filter, & Lopez Filters for all P & L band images. The Classification accuracies are low and comparable for C-Band frequencies. It can be particularly noted that the classification accuracy values are higher for the P and L-Band PolSAR images as compared with the C-band PolSAR images.

VI. CONCLUSIONS

The multi-frequency study of the fully polarimetric morphological filter reveals that the classification accuracies are high for the P & L-band PolSAR images. However, the best classification accuracies are achieved with the L-Band PolSAR images. Also, from the metrics used for visual quality inspection it can be observed that the values of SSIM, and MSSSIM are high enough. This indicates that the edges are largely preserved thus helping in improving the visual quality of the filtered image. The proposed method can be used to remove speckle noise to a good extent, while preserving point targets and structural similarities. The morphological filter works well even if the number of classes is large. The image quality metrics show that the first opening and closing operation removes most of the speckle. The following opening and closing operations contribute less to noise removal and may eliminate some point targets completely. Hence the number of opening and closing operations can be restricted to only one. Since the fully polarimetric morphological filter works well with the L-Band PolSAR images, this technique of filtering can be used to process the images acquired from the L-Band PolSAR images from the NISAR mission. In the future we would like to test the filter using unsupervised methods based on various decomposition techniques. It is expected that the proposed fully polarimetric speckle filter based on morphological operations might give better classification accuracies using image decomposition techniques.

REFERENCES

- [1] S.-W. Chen, "SAR Image Speckle Filtering with Context Covariance Matrix Formulation and Similarity Test," *IEEE Trans. Image Process.*, vol. 7149, no. c, pp. 1–1, 2020.
- [2] M. Yahia, T. Ali, M. M. Mortula, R. Abdelfattah, and S. El Mahdy, "Polarimetric SAR Speckle Reduction by Hybrid Iterative Filtering," *IEEE Access*, vol. 8, pp. 89603–89616, 2020.
- [3] Butkar, M. U. D., & Waghmare, M. J. (2023). Hybrid Serial-Parallel Linkage Based six degrees of freedom Advanced robotic manipulator. *Computer Integrated Manufacturing Systems*, 29(2), 70-82.
- [4] L. Ashok Kumar and M. R. Ebenezer Jebarani, "A comprehensive review on speckle denoising techniques in satellite images," *Proc. 2019 IEEE Int. Conf. Commun. Signal Process. ICCSP 2019*, pp. 245–248, 2019.
- [5] S. W. Chen, X. S. Wang, S. P. Xiao, and M. Sato, "General polarimetric model-based decomposition for coherency matrix," *IEEE Trans. Geosci. Remote Sens.*, vol. 52, no. 3, pp. 1843–1855, 2014.
- [6] Butkar, U. (2014). A Fuzzy Filtering Rule Based Median Filter For Artifacts Reduction of Compressed Images.
- [7] J. Sen Lee, J. H. Wen, T. L. Ainsworth, K. S. Chen, and A. J. Chen, "Improved sigma filter for speckle filtering of SAR imagery," *IEEE Trans. Geosci. Remote Sens.*, vol. 47, no. 1, pp. 202–213, 2009.
- [8] Uamakant, B., 2017. A Formation of Cloud Data Sharing With Integrity and User Revocation. *International Journal Of Engineering And Computer Science*, 6(5), p.12.
- [9] R. Touzi, "A review of speckle filtering in the context of estimation theory," *IEEE Trans. Geosci. Remote Sens.*, vol. 40, no. 11, pp. 2392–2404, 2002.
- [10] A. Kher and S. Mitra, "Efficient speckle removing algorithm based on new morphological operators," *Midwest Symp. Circuits Syst.*, vol. 2, pp. 852–855, 1994.
- [11] G. Singh *et al.*, "Seven-Component Scattering Power Decomposition of POLSAR Coherency Matrix," *IEEE Trans. Geosci. Remote Sens.*, vol. 57, no. 11, pp. 8371–8382, 2019.
- [12] D. Ma, X. Zhang, X. Tang, J. Ming, and J. Shi, "A CNN-Based Method for Sar Image Despeckling," *Int. Geosci. Remote Sens. Symp.*, pp. 4272–4275, 2019, doi: 10.1109/IGARSS.2019.8899122.
- [13] Cameron, W.L., Youssef, N., and Leung, L.K. 1996. Simulated polarimetric signatures of primitive geometrical shapes. *IEEE Transactions on Geoscience and Remote Sensing*, Vol. 34, No. 3, pp. 793–803.
- [14] Cloude, S.R., and Pottier, E. 1996. A review of target decomposition theorems in radar polarimetry. *IEEE Transactions on Geoscience and Remote Sensing*, Vol. 34, No. 2, pp. 498–518.
- [15] Corr, D.G., and Rodrigues, A.F. 2002. Alternative basis matrices for polarimetric decomposition. In *EUSAR 2002, Proceedings of the 4th European Union Conference on Synthetic Aperture Radar*, 4–6 June 2002, Cologne, Germany.
- [16] Butkar, U. (2016). Review On-Efficient Data Transfer for Mobile devices By Using Ad-Hoc Network. *International Journal of Engineering and Computer Science*, 5(3).
- [17] Karam, M.A., Amar, F., Fung, A.K., Mougin, E.,

- Lopes, A. LeVine, D.M., and Beaudoin A. 1995. A polarimetric scattering model for forest canopies based on vector radiative transfer theory. *Remote Sensing of Environment*, Vo. 53, pp. 16-30.
- [18] Lee, J.S., Schuler, D.L., Ainsworth, T.L., Krogager, E., Kasilingam, D., and Boerner, W.-M. 2002. On the estimation of radar polarization orientation shifts induced by terrain slopes. *IEEE Transactions on Geoscience and Remote Sensing*, Vol. 49, No.1, pp. 30-41.
- [19] Butkar, U. (2014). An execution of intrusion detection system by using generic algorithm.
- [20] Touzi, R., and Charbonneau, F. 2002. Characterization of target symmetric scattering using polarimetric SARs. *IEEE Transactions on Geoscience and Remote Sensing*, Vol. 40, pp. 2507–2516.
- [21] Van Zyl, J.J. 1989. Unsupervised classification of scattering behavior using radar polarimetry data. *IEEE Transactions on Geoscience and Remote Sensing*, Vol. 27, No. 1, pp. 37–45.
- [22] Yamaguchi, Y., Moriyama, T., Ishido, M., and Yamada, H. 2005. Four-component scattering model for polarimetric SAR image decomposition. *IEEE Transactions on Geoscience and Remote Sensing*, Vol. 43, No. 8, pp. 1699–1706.
- [23] G. Singh *et al.*, “Seven-Component Scattering Power Decomposition of POLSAR Coherency Matrix,” *IEEE Trans. Geosci. Remote Sens.*, vol. 57, no. 11, pp. 8371–8382, 2019.

VIII. acknowledgements

This work is partially supported by “Vidyalankar Institute of Technology”, Wadala, Mumbai, India, under the scheme of “Higher Studies Sponsorship Policy”, Year 2024.